

Platelets and Pro-Angiogenic Circulating Cells Accelerate Skin Wound Healing

Silvia Erratico

Novystem Spa, viale Piave 21, 20129 Milan, Italy

Marzia Belicchi

Stem Cell Laboratory, Department of Pathophysiology and Transplantation, Università degli Studi di Milano, Unit of Neurology, Fondazione IRCCS Ca' Granda Ospedale Maggiore Policlinico, Centro Dino Ferrari, via Francesco Sforza 35, 20122 Milan, Italy

Mirella Meregalli

Stem Cell Laboratory, Department of Pathophysiology and Transplantation, Università degli Studi di Milano, Unit of Neurology, Fondazione IRCCS Ca' Granda Ospedale Maggiore Policlinico, Centro Dino Ferrari, via Francesco Sforza 35, 20122 Milan, Italy

Dario Di Silvestre

Institute of Technologies in Biomedicine, National Research Council (ITB-CNR), Via Fratelli Cervi, 93, 20090 Segrate, Milan, Italy

Luana Tripodi

Novystem Spa, viale Piave 21, 20129 Milan, Italy

Antonella De Palma

Institute of Technologies in Biomedicine, National Research Council (ITB-CNR), Via Fratelli Cervi, 93, 20090 Segrate, Milan, Italy

Rebecca Jones

Department of Molecular Biotechnology and Health Science, University of Torino, Via Nizza 52 10126 Torino, Italy

Emanuele Ferrari

Institute of Technologies in Biomedicine, National Research Council (ITB-CNR), Via Fratelli Cervi, 93, 20090 Segrate, Milan, Italy

Lura Porretti

Flow Cytometry Service, Fondazione IRCCS Ca' Granda Ospedale Maggiore Policlinico, via Francesco Sforza 35, 20122 Milan, Italy

Elena Trombetta

Flow Cytometry Service, Fondazione IRCCS Ca' Granda Ospedale Maggiore Policlinico, via Francesco Sforza 35, 20122 Milan, Italy

Giorgio R. Merlo

Department of Molecular Biotechnology and Health Science, University of Torino, Via Nizza 52 10126 Torino, Italy.

Pierluigi Mauri

Institute of Technologies in Biomedicine, National Research Council (ITB-CNR), Via Fratelli Cervi, 93, 20090 Segrate, Milan, Italy

Yvan Torrente (✉ yvan.torrente@unimi.it)

Stem Cell Laboratory, Department of Pathophysiology and Transplantation, Università degli Studi di Milano, Unit of Neurology, Fondazione IRCCS Ca' Granda Ospedale Maggiore Policlinico, Centro Dino Ferrari, via Francesco Sforza 35, 20122 Milan, Italy <https://orcid.org/0000-0002-2705-3984>

Research

Keywords: wound healing, PRP, angiogenic potential, skin regeneration, ECM remodeling

Posted Date: January 20th, 2021

DOI: <https://doi.org/10.21203/rs.3.rs-148617/v1>

License:   This work is licensed under a Creative Commons Attribution 4.0 International License.

[Read Full License](#)

Abstract

Background

Delayed wound healing and chronic skin lesions represent a major health problem. Over the past years, growth factors mediated by platelet-rich plasma (PRP) and cell-based therapies were developed as effective and affordable treatment able to improve wound healing capacity. However, the precise molecular mechanism through which PRP exhibits its beneficial effects remains unrevealed. Herein we show that a combination of PRP and pro-angiogenic cells (Angio^{PRP}) could exert a synergistic positive effect on keratinocyte proliferation and angiogenesis accelerating wound healing.

Method

We designed a sterile and closed class IIa device (NovySep) for single use only to collect blood-derived mononucleated cells and the plasma phase after centrifugation without opening the system. We performed in vitro and in vivo wound healing experiments to assess the angiogenic potential of Angio^{PRP}; we evaluated the extracellular matrix remodeling and the physical properties of treated wounds through mechanical (stress-strain test) and proteomics analysis.

Result

Angio^{PRP} enhanced wound healing by promoting uniform regeneration of the basal and granular layers and vessel remodeling. We coupled this effect with normalization of mechanical properties of rescued mouse wounds, which is sustained by a correct arrangement of elastin and collagen fibers. The network analysis-based protein–protein interactions of Angio^{PRP}-treated wounds demonstrated a fingerprint of Angio^{PRP}-related proteins that may provide the signal for a faster wound healing response which include Caveolin and EGFR/TGF β / β -catenin pathways.

Conclusion

A combined treatment composed of PRP and a pool of pro-angiogenic/keratogenic cells (Angio^{PRP}) may provide a more integrated method to supports wound healing, by promoting a cascade of events leading to the reduction of TGF β 1/ β -catenin up-downstream signaling pathways. The molecular mechanism undergoing the support of Angio^{PRP} to wound healing opens new perspectives in the treatment of skin injuries.

Background

Wound healing is a dynamic and orchestrated sequence of events requiring the interaction of soluble mediators, blood cells and extracellular matrix that result in the restoration of skin integrity and homeostasis [1]. Wound repair proceeds in three overlapping and functionally distinct phases characterized first by infiltration of neutrophils and macrophages, [2] followed by angiogenesis,

fibroblasts and keratinocytes proliferation[3] that allows granulation tissue formation and extracellular matrix remodeling [4, 5]. An interruption in the normal wound healing process can lead to the development of non-healing chronic wounds, a typical complication of several diseases, such as foot ulcer from diabetes and pressure ulcer resulting from spinal cord injuries [6]. As wound healing impairment represents a major health problem, the complexity of cell and molecular events required for appropriate repair constitute a major research focus.[7, 8] In this regard, different dressing and ointments such as hydrocolloids, alginates, foams, sulfadiazine silver patches, and honey gauzes have been described to promote chronic wound healing [9]. Nevertheless, the systematic review [10] of local interventions do not support conclusive evidences for ulcer healing. Other evidences suggest that hyperbaric oxygen and negative pressure wound therapy systems can induce and accelerate wound healing [11]; however these interventions are limited by reduced availability, patients' intolerance and high costs. For extensive wounds, a variety of skin substitutes are available, that can be classified by origin (allogenic, xenogeneic, and autologous), composition (dermal, epidermal or both components) or timing (durable or temporary substitutes) [12, 13]. The ideal skin substitute performs the functions of skin, while being cost-effective, widely available, and easy to apply.[14] Platelet-rich plasma (PRP) has shown promising experimental and clinical results in chronic wound. Moreover, application of PRP has been demonstrated to be effective in soft tissue reconstruction [15, 16], bone reconstruction [17, 18] and hair regrowth [19–22]. The addition of bioactive excipients, both natural as fat graft and synthetic (i.e. hyaluronic acid, 3D collagen scaffolds) has also been suggested to accelerate endothelial, epithelial and epidermal regeneration of PRP [15, 17, 23, 24]. The major families of growth factors that are released from PRP and are involved in wound healing includes factors that stimulates fibroblasts to secrete collagenases during the remodeling phase and encourages keratinocyte and fibroblast proliferation [25]. Increased rates of cell proliferation and cell migration have been associated with the upregulation of different cell-cycle-regulatory proteins and PI3K/AKT/NF- κ B signaling pathways [26, 27]. Although PRP is a source of growth factors, and consequently has mitogenic, angiogenic, and chemotactic properties, representing an interesting alternative adjunctive treatment for acute and chronic wounds, PRP is far from standardized and the most effective way of application has yet to be defined. Further, commercial PRP separation systems vary widely regarding the harvest and concentration of various PRP substances. Chronic wounds also occur with complications of impaired angiogenesis [28, 29] and transplantation of endothelial progenitor cells (EPCs) has demonstrated promising results in wound healing [30]. EPCs are bone marrow mononuclear progenitor cell that were first discovered as circulating cells in peripheral blood [31, 32] and characterized for their capacity to increase angiogenesis and vascularization by secreting growth factors and cytokines in damaged tissues [33]. Circulating EPCs displayed specific cell surface markers such as CD45 to identify their hematological origin in combination with different endothelial surface markers, such as CD31, CD144 or CD146 [34, 35]. Recent studies suggest that angiogenic T-cells (Tangs) may regulate EPC function [36–38]. Tang express CD31 as well as the receptor for stromal derived factor 1 (CD184) [38] and promote the formation of new blood vessels and endothelial repair by stimulating the function of EPC [38].

Based on the above, it is reasonable to speculate that a combination of PRP and pro-angiogenic cells could exert a synergistic positive effect on keratinocyte proliferation and angiogenesis accelerating wound healing. To achieve this goal, we created a single-use class IIa device for the contemporary isolation of human PRP and circulating EPCs and Tregs (hereafter named $\text{Angio}^{\text{PRP}}$) and investigated their role in enhancing the *in vitro* and *in vivo* wound healing process. The regulation and mechanism of $\text{Angio}^{\text{PRP}}$ on wound healing efficiency *in vivo* were investigated. Since human $\text{Angio}^{\text{PRP}}$ can be prepared from autologous peripheral blood, our findings may lead to the development of novel therapeutic interventions for various angiogenesis-related diseases as well as to the improvement of strategies for tissue engineering and organ regeneration.

Methods

Methods

$\text{Angio}^{\text{PRP}}$ isolation and characterization.

We designed a sterile and closed class IIa device (NovySep), characterized by a collecting tube with an inert porous membrane of high-grade polyethylene, a rubber stopper to insert peripheral blood with a 2.5 ml syringe needle (21G) and a ring nut to adjust the plasma phase volume above the membrane after centrifugation (Fig. 1A). The device was designed for single use only and to collect blood-derived mononucleated cells and the plasma phase after centrifugation without opening the system. Peripheral blood was collected from healthy volunteers ($n = 101$) of the blood bank of Department of Transfusion Medicine and Haematology at Policlinico Hospital of Milan, after informed consent and according to the guidelines approved by the Ethics Committee on the Use of Human Subjects in Research of the Policlinico Hospital of Milan (Milan, Italy, Ethics Committee permission number 793/13). 2.5 ml of peripheral blood, collected in sodium citrate tube were filled into NovySep device and centrifuged at 1500 rpm for 10 minutes to induce the phase separation (EP20161201.7). The platelet-rich-plasma phase (PRP) and the cells at the interface between red cells and plasma were collected. We analysed pre-separation blood and $\text{Angio}^{\text{PRP}}$ by blood Coulter counter instrument (DxH 500, Beckman Coulter). Pre-separation blood and cell phase collected were directly labelled with monoclonal antibodies shown below. Cells were incubated with Syto 16, anti-CD45 V500, anti-CD3 V450, anti-CD3 APC, anti-CD56 PE-CY7, anti-CD14 APC-H7, anti-CD16 PE, anti-CD15 V450, anti-CD19 APC-R700 or anti-CD31 PE Cy7, anti-CD184 APC, anti-CD90 PerCP, anti-CD90 FITC, anti-CD146 PE, anti-CD34 APC (BD Biosciences-Pharmingen, San Diego, California, USA). The controls were isotype-matched mouse immunoglobulins. After each incubation performed at 4 °C for 20 minutes, cells were washed in PBS 1X containing 1% heat-inactivated FCS and 0,1% sodium azide. The cytometric analyses were performed on a LYRIC flow cytometer using FACSuite software (BD Biosciences-Immunocytometry System). Each analysis included at least $1-2 \times 10^4$ events for each gate. A light-scatter gate was set up to eliminate cell debris from the analysis. The percentage of positive cells was assessed after correction for the percentage reactive to an

isotype control conjugated to a specific fluorophore. Percentage of different cells subpopulations were calculated on the Syto 16 positive gate.

Ex vivo preclinical experimentation: EPC colony forming assay, HUVEC coculture and organotypic skin culture.

The angiogenic potential of Angio^{PRP} was tested in 35-mm dishes using the Endothelial Progenitor Cell Colony-Forming Assay (EPC-CFA) (MethoCult SFBIT; STEMCELL Technologies Inc.) added with proangiogenic growth factors/ cytokines, as previously reported [39] (rh SCF 100 ng/ml, rh VEGF 50 ng/ml, rh b-FGF 50 ng/ml, rh EGF 50 ng/ml and rh IGF-1 ng/ml, all from Miltenyi Biotec; eparin 2 U/ml, STEMCELL Technologies Inc). Aliquots of Angio^{PRP} were seeded at a cell density of 5×10^4 cells/dish (3 dishes per volunteer). 16 to 18 days after the beginning of the culture, the number of adherent EPC colonies per dish was counted under phase contrast light microscopy LEICA DMi8 (Leica, Germany). Primitive EPC colony-forming units (pEPC-CFUs) and definitive EPC-CFUs (dEPC-CFUs) were separately counted and expressed as a percentage of the total number. Pro-angiogenic potential of Angio^{PRP} was evaluated in coculture system constructed using human umbilical vein endothelial cells (HUVECs) as previously described.[40] Briefly, 8×10^4 HUVEC (ATCC-LGC, VA, USA) were plated on 3D Matrigel (BD Biosciences-Pharmingen, San Diego, California, USA); 1.35×10^5 cells and 9.55×10^6 platelets for Angio^{PRP} or 9.55×10^6 platelets for PRP were added to HUVEC culture; after 24 hours cells ramification was quantified by ImageJ software (NIH) [41]. To investigate the skin regeneration potential of Angio^{PRP}, we used a multilayered model of human dermis and epidermis as previously described (MatTek's EpiDermFT Full Thickness EFT-400) [42]. Epidermal-only wounds were induced using a sterile 5 mm dermal biopsy punch (Miltex Inc., York, PA) and the epidermis was mechanically removed using forceps. After wounding, EpiDermFT tissues were cultured into 6-well plate with four different culture conditions: 1) an organotypic skin culture with 3.5×10^4 cells and 9.85×10^6 platelets for complete Angio^{PRP}, 2) 3.5×10^4 cells of Angio^{cells} suspended in PBS, 3) 9.85×10^6 platelets for PRP, 4) 50 μ l of PBS 1X (as negative control) and analyzed after 24 hours, 2, 4, 5, 6 and 7 days of culture. Blood from 10 healthy volunteers was collected in NovySep device to obtain 10 individual Angio^{PRP} as described above. The isolated 10 Angio^{PRP} were pooled and further centrifuged at 1500 rpm for 10 minutes to obtain a pellet of cells which was suspended in PBS (Angio^{cells}). The supernatant containing platelets rich plasma (PRP) was used as such. Wound closure was calculated via equation:

Wound healing (%) = $(1 - \text{Open wound area} / \text{Initial wound area}) \times 100$

In vivo wound healing experiments.

Five-month-old severe combined immunodeficient (NOD.Cg-Prkdc^{Scid}/J) [43] mice were obtained from Charles River Laboratories International, Inc. (Calco, Italy); the use of animals in this study was authorized by the National Ministry of Health (authorization number 51/2018-PR). All experimental protocols were reviewed and approved by the University of Torino's animal ethics research committee. The methods described below were carried out in accordance with those approved protocols, as well as the Italians

ethical guidelines regarding the use of experimental animals. Wound healing model was obtained as described in Dunn and colleagues [44]. Briefly, animals were anesthetized with avertin and two full-thickness excisions of 5-mm that include the panniculus carnosus were created on the dorsum, one on each side of the midline of the mouse. A silicone splint was placed around the wound with the assistance of adhesive and the splint was then secured with interrupted sutures. Each mouse acts as its own control, with one wound receiving treatment (Angio^{PRP} or Hyalomatrix, Anika Therapeutics Inc., Bedford, MA 01730, USA) and the other phosphate buffer saline (PBS 1X). A transparent occlusive dressing was applied to prevent contamination. Wounds were checked by taking photos every 2–3 days, and the area was quantified relative to a millimeter reference using ImageJ software (NIH) and expressed as the percentage of wound area measured at day 0, 4, 7, 10, 15 and 21 days after injury, corresponding to wound closure; mice were sacrificed by cervical dislocation under full deep anesthesia and the back skin lesions were removed; the biopsies have been divided into two group respectively for histological or proteomic analysis. One group was placed in isopentane and freezed at -80 °C for proteomic analysis. The other group was incubated in 4% paraformaldehyde in PBS at 4 °C overnight and after transferred to 30% sucrose in PBS 1X solution for a further 24 hours at 4 °C, embedded in O.C.T matrix and freezed at -80 °C. Serial sections of 12 µm thickness were cut and examined by immunofluorescence and histological analysis.

Histological and immunofluorescence stainings.

Serial section of 12 µm of skin tissue and organotypic skin were cut and stained with hematoxylin and eosin (H&E, Bio Optica Spa, Italy) Orcein (Sigma-Aldrich Inc., St. Louis, MO, USA) and Masson's trichrome staining (Bio Optica Spa, Italy), according to the manufacturer's instructions for morphological assessment. Images were captured with LMD6000B (Leica, Germany) at 12 regular intervals, representing the entire section and the epidermal thickness was quantified as area per interval using ImageJ software (<http://rsbweb.nih.gov/ij/>). For immunofluorescence analysis, transversal tissue sections were incubated with mouse monoclonal antibody anti-Citokeratin 10 (1:100, ab9025, Abcam, UK), rabbit monoclonal antibody anti-Vimentin (1:100, ab16700, Abcam, UK), rabbit polyclonal antibody anti-Involucrin (1:100, ab53112, Abcam, UK), mouse monoclonal antibody anti-Cytokeratin 14 (1:100, ab7800 Abcam, UK) rabbit polyclonal antibody anti-Cytokeratin 5 (1:100, ab53121, Abcam, UK), rabbit polyclonal antibody anti-β-Catenin (1:200, ab16051, Abcam, UK), rabbit polyclonal antibody anti-CD206 (1:200, ab64693, Abcam, UK), Alexa Fluor 594 rat monoclonal antibody anti-Ly-6G/Ly-6C (Gr-1)(1:50, 108448 BioLegend), rat monoclonal antibody anti-CD31 (1:50, 550274 BD Biosciences-Pharmingen, San Diego, California, USA), rabbit polyclonal antibody anti-Collagen VI (1:250, ab6588, Abcam, UK), mouse monoclonal antibody anti-alpha SMA (1:50, A2547, Sigma-Aldrich Inc., St. Louis, MO, USA), rabbit polyclonal antibody anti-VE-Cadherin (1:50, ab33168, Abcam, UK), mouse monoclonal antibody anti-eNOS (1:100, ab76198, Abcam, UK), rat monoclonal anti-E-Cadherin (1:100, ab11512, Abcam, UK), mouse monoclonal anti-Cytokeratin 10 (1:100, ab9025, Abcam, UK), rabbit polyclonal anti-Loricrin E-Cadherin (1:100, ab85679, Abcam, UK). Cell nuclei were stained for 5 min at room temperature with DAPI (Sigma-Aldrich Inc., St. Louis, MO, USA). Slides were analyzed using a fluorescent microscope LEICA DMI8 (Leica, Germany), images were

captured at regular intervals along the entire section and fluorescence intensity per single interval was quantified with Image J software (<http://rsbweb.nih.gov/ij/>); integrated density was measured using a ROI corresponding to epidermal region in each slice interval and plotted in the graphic after subtracting the corresponding background signal measured within the tissue-free area [45].

Strength Measurements.

Following sacrifice, the skins for mechanical testing were placed in metal screw clamps with rubber pieces covering the clamped ends. Clamps were placed into a Bose Electroforce 3100 instrument. Applying an initial traction of 0.15 N, the traction measured in MPa was increased by 0.2% per second up to the breaking point. Force (N) and displacement (mm) were measured on a *xy* plotter and these points were subsequently recorded as stress (σ = force per cross-sectional area) and strain (ϵ = change in length/initial length) and re-plotted in Excel [46].

Western Blot analysis.

WB analysis were performed as previously described [47]. Briefly, total proteins from skin tissue of five-month-old severe combined immunodeficient (NOD.Cg-Prkdc^{Scid}/J) mice were extracted and quantified with Bradford Assay. Samples were resolved on polyacrylamide gels (ranging from 10–14%) and transferred to nitrocellulose membranes (Bio-Rad Laboratories, California, USA). Filters were incubated overnight with following antibodies: Vinculin (1:600, MA5-11690 Thermo Fisher Scientific, MA, USA); TGF β (Rb pAb 1:600, ab92486, Abcam, UK); β -Catenin (Rb pAb 1:600, ab16051, Abcam, UK); Membranes were incubated with primary antibodies ON at 4 °C, then followed by washing, detection with horseradish peroxidase (HRP)-conjugated secondary antibodies (Dako Agilent, CA, USA) and developed by enhanced chemiluminescence (ECL) (Amersham Biosciences, USA). Bands were visualized using an Odyssey Infrared Imaging System (Li-COR Biosciences, USA). Densitometric analysis was performed using ImageJ software (<http://rsbweb.nih.gov/ij/>).

Proteomics analysis.

In-solution digestion

For proteomic analysis the epidermal and dermal layers of the treated skin enclosed by the silicone splint were removed 21 days after injury and frozen in isopentane. Samples were then suspended in 200 μ L 0.1 M NH₄HCO₃ pH 7.9 buffer and homogenized in ice. The protein concentration was assayed using SPN-Protein assay kit (G-Biosciences, St. Louis, MO, USA) and the membrane proteins were solubilized by adding Rapigest SF reagent (Waters Co, Milford, MA, USA) at the final concentration of 0.2% (*w/v*). The resulting suspensions were incubated under stirring at 100 °C for 20 minutes and at 80 °C for 2 hours. The digestion was carried out on 50 \pm 0.5 μ g proteins of each sample by adding Sequencing Grade Modified Trypsin (Promega Inc., Madison, WI, USA) at an enzyme/substrate ratio of 1:50 (*w/w*) overnight at 37 °C in 0.1M NH₄HCO₃ pH 7.9 buffer with 10% CH₃CN. An additional aliquot of 0,5 μ g of trypsin (1:100 *w/w*) was added in the morning, and the digestion continued for 4 hours. Moreover, the addition of

0.5% Trifluoroacetic acid (TFA) (Sigma-Aldrich Inc., St Louis, MO, USA) stopped the enzymatic reaction, and a subsequent incubation at 37 °C for 45 min completed the RapiGest acid hydrolysis [48]. The water immiscible degradation products were removed by centrifugation at 13.000 rpm for 10 minutes. Finally, the tryptic digest mixtures were desalted using Pierce C-18 spin columns (Thermo Fisher Scientific - Pierce Biotechnology, Rockford, IL, USA), according to manufacturer protocol and were resuspended in 0.1% formic acid (Sigma-Aldrich Inc., St. Louis, MO, USA) in water (LC-MS Ultra CHROMASOLV, Honeywell Riedel-de Haen, Muskegon, MI, USA).

LC-MS/MS

Analysis were performed as previously described [49]. Briefly, trypsin digested mixtures were analyzed using Eksigent nanoLC-Ultra 2D System (Eksigent, part of AB SCIEX Dublin, CA, USA) combined with cHiPLC-nanoflex system (Eksigent) in trap-elute mode. Briefly, samples (0.8 µg injected) were first loaded on the cHiPLC trap (200 µm x 500 µm ChromXP C18-CL, 3 µm, 120 Å) and washed with the loading pump running in isocratic mode with 0.1% formic acid in water for 10 minutes at a flow of 3 µL/min. The automatic switching of cHiPLC ten-port valve then eluted the trapped mixture on a nano cHiPLC column (75 µm x 15 cm ChromXP C18-CL, 3 µm, 120 Å) through a 87 minutes gradient of eluent B (eluent A, 0.1% formic acid in water; eluent B, 0.1% formic acid in acetonitrile) at a flow rate of 300 nL/min. In depth, gradient was: from 5–10% B in 3 min, 10–40% B in 80 min, 40–95% B in 17 min and holding at 95% B for 7 min. Trap and column were maintained at 35 °C for retention time stability. Mass spectra were acquired using a QExactive mass spectrometer (Thermo Fisher Scientific, San José, CA, USA), equipped with an EASY-Spray ion source (Thermo Fisher Scientific, San José, CA, USA). Easy spray was achieved using an EASY-Spray Emitter (Dionex Benelux BV, Amsterdam, The Netherlands) (nanoflow 7 µm ID Transfer Line 20 µm x 50 cm) held to 1.9 kV, while the ion transfer capillary was held at 220 °C. Full mass spectra were recorded in positive ion mode over a 400–1600 m/z range and with a resolution setting of 70000 FWHM (@ m/z 200) with 1 microscan per second. Each full scan was followed by 10 MS/MS events, acquired at a resolution of 17,500 FWHM, sequentially generated in a data dependent manner on the top ten most abundant isotope patterns with charge ≥ 2 , selected with an isolation window of 2 m/z from the survey scan, fragmented by higher energy collisional dissociation (HCD) with normalized collision energies of 30 and dynamically excluded for 10 sec. The maximum ion injection times for the survey scan and the MS/MS scans were 100 and 200 ms and the ion target value were set to 10^6 and 10^5 , respectively.

Data Analysis

All data generated were searched using the Sequest HT search engine contained in the Thermo Scientific Proteome Discoverer software, version 2.1. The experimental MS/MS spectra were correlated to tryptic peptide sequences by comparison with the theoretical mass spectra obtained by in silico digestion of the Uniprot Mus musculus proteome database (54109 entries), downloaded in February 2019 (www.uniprot.org). The following criteria were used for the identification of peptide sequences and related proteins: trypsin as enzyme, three missed cleavages per peptide, mass tolerances of ± 10 ppm for precursor ions and ± 0.6 Da for fragment ions. Percolator node was used with a target-decoy strategy to

give a final false discovery rates (FDR) at Peptide Spectrum Match (PSM) level of 0.01 (strict) based on q-values, considering maximum deltaCN of 0.05 [50]. Only peptides with high confidence, minimum peptide length of six amino acids, and rank 1 were considered. Protein grouping and strict parsimony principle were applied.

Label-free differential analysis

In order to improve the identification of differentially expressed proteins, two different and complementary label-free approaches were adopted: an in-house algorithm, Multidimensional Algorithm Protein Map (MAProMa)[51] and Linear Discriminant Analysis (LDA). The protein lists obtained from the SEQUEST algorithm were aligned and compared by means of the average spectral counts (aSpC), corresponding to the average of all the spectra identified for a protein and, consequently, to its relative abundance, in each analyzed condition (Healthy, PBS control, Angio^{PRP}, Hyalomatrix). In depth, to select differentially expressed proteins, subgroups were pairwise compared, applying a threshold of 0.2 and 5 on the two MAProMa indexes DAve (Differential Average) and DCI (Differential Confidence Index), respectively. DAve, which evaluates changes in protein expression, was defined as $(X-Y)/(X+Y)/0.5$, while DCI, that evaluates the confidence of differential expression, was defined as $(X+Y) \times (X-Y)/2$. The X and Y terms represent the SpC of a given protein in two compared samples.

Linear Discriminant Analysis and Hierarchical Clustering

The average SpC (aSpC) values of the identified proteins were calculated by MAProMa software. The spectral count (SpC) values were normalized using a total signal normalization method and compared using a label-free quantification approach, as previously reported.[52] In detail, the considered protein lists (D, n = 6; AC, n = 6; BC, n = 6; A, n = 6; B, n = 6) were first processed by linear discriminant analysis (LDA) and proteins with the largest (≥ 4) F ratio and smallest P-value (≤ 0.01) were retained and considered differentially expressed with high confidence. Proteins selected by LDA were processed by hierarchical clustering applying Ward's method and a Euclidean distance metric using JMP15 software.

Proteome remodeling index

Proteome Recovery and Proteome Activation Index For each protein it was evaluated its variations (modules) due to perturbation (Healthy, D, vs. Disease, C(B)) and/or treatment (Disease, C(B) vs. treatment, A); if the two modules present similar values but opposite sign, the protein recovers its level to the reference (in our case Healthy condition). The extraction of so-called "recovered proteins" was simplified by calculating the Proteome Remodeling index (PRi) for each protein using an unbiased procedure. The PRi is calculated by the following formula:

$$PRi = M(b-p)J/M(p-t)J$$

where J: each identified protein;

M(b-p)J: Perturbation Module = Difference Healthy vs. Disease

(b: baseline; p: perturbed);

differential abundance of specific protein J comparing healthy (D) vs. Disease (C(B)) conditions.

M(p-t)J: Treatment Module = Difference Disease vs. treatment

(t: treated, A)

differential abundance of specific protein J comparing perturbed (disease) vs. treated (A) conditions.

Theoretically, if protein level after treatment remodeled to reference (healthy) the two modules (perturbation and treatment) should have similar value and opposite sign; then the PRi will be negative and close to unit (-1). In our case, we considered proteins with a PRi in the range - 0.5 to -2. Differential abundance of each module may be expressed as DAVE value, from MAProMa algorithm or $\ln[\text{fold change}]$. However, because in some cases the fold-change calculation returns non-sense values (such as $n/0$ or $0/n$), we preferred to use DAVE value to calculate modules. Moreover, MAProMa platform permits the filtration by absolute variation, using DCI algorithm, excluding very low expressed protein (very low spectral count, multiple $\text{DCI} < |5|$) confusingly with noise [49, 53].

Network analysis

A protein-protein interaction (PPI) network was built by combining differentially expressed proteins and the Mus Musculus PPI network retrieved from STRING database; only experimentally and database defined PPI with a score > 0.15 were considered. The resulting sub-networks were visualized and analyzed by Cytoscape and its plugins, as previously reported [54]. Specifically, BINGO 2.44 Cytoscape plugin[55] was used for evaluating the most represented GO terms; Mus musculus organism, hypergeometric test, Benjamini–Hochberg FDR correction and a significance level ≤ 0.01 were applied.

Statistics

Sample size was determined considering a statistical test power of 0.80 and an alpha value of 0.05. Results indicated that a sample size of 15 animals ($n = 5$ per group) would enable to detect a minimum difference in protein expression of 0.35 with an expected standard deviation of 0.15. To detect outliers, Grubb's test was applied for each parameter. A probability value < 0.05 was considered significant. All analyses were performed as previously described [49] using Sigma Stat 11.0 dedicated software (Systat Software Inc., San Jose, CA, USA). Identified proteins were evaluated by LDA (JMP15 software SAS; F ratio > 4 and a p-value < 0.01) and MAProMa platforms. Finally, proteins extracted by PRi algorithms were statistically evaluated by ANOVA and Tukey's test.

Results

Angio^{PRP} is prevalently enriched of platelets and peripheral CD45+/CD31+/CD34- blood cells with Tang and EPC features.

Separation of peripheral blood was performed through NovySep device and the $\text{Angio}^{\text{PRP}}$ was analysed to characterize the cell and platelet composition (Fig. 1a). As expected, $\text{Angio}^{\text{PRP}}$ is composed mainly by platelets ($88.92 \pm 7.001\%$) with a low amount of white blood cells (WBCs) ($0.34 \pm 0.29\%$) (Fig. 1b). The platelets concentration is significantly increased in $\text{Angio}^{\text{PRP}}$ compared to the whole-blood before preparation ($133.6 \pm 49.78 \times 10^3$ instead of $109.6 \pm 39.95 \times 10^3$ platelets/ μl , Fig. 1c), while WBCs are significantly decreased ($0.47 \pm 0.39 \times 10^3$ instead of $4.27 \pm 1.17 \times 10^3$ WBC/ μl , Fig. 1d) ($n = 101$; paired t-test $p < 0.0001$). Moreover, Coulter counter analysis demonstrated that $\text{Angio}^{\text{PRP}}$ is significantly enriched of lymphocytes compared to the whole-blood hold before preparation ($67.15 \pm 9.25\%$ for $\text{Angio}^{\text{PRP}}$ and $29.98 \pm 6.52\%$ for whole blood), while the granulocyte population is severely reduced ($12.32 \pm 7.67\%$ for $\text{Angio}^{\text{PRP}}$ and $62.36 \pm 7.38\%$ for whole blood) and monocytes partially increased ($20.13 \pm 6.30\%$ for $\text{Angio}^{\text{PRP}}$ and $7.69 \pm 1.56\%$ for whole blood, Fig. 1e) ($n = 25$, multiple t-test, $p < 0.0001$). In these analysis the cellular component of $\text{Angio}^{\text{PRP}}$ was discriminated from the red blood cells and platelets using CD41a and Glycophorin A labeling (double negative population in Fig. 1f); cytometric characterization of $\text{Angio}^{\text{PRP}}$ highlighted the immunophenotype of double negative CD41a and Glycophorin A cells as CD45+/CD31+/CD34- ($89.99 \pm 8.86\%$; $n = 19$, Fig. 1g). Among these cells we identified distinct subpopulations of lymphocytes ($55.43 \pm 10.97\%$ of T cells, $20.57 \pm 5.85\%$ of Tregs as T cell subpopulation with angiogenic potential and $13.84 \pm 4.92\%$ of B cells), CD146+/90+/31+ EPCs ($0.60 \pm 0.52\%$), natural killers (NKs, $6.56 \pm 3.52\%$), monocytes ($5.46 \pm 2.18\%$ of CD14+/CD16- and $4.88 \pm 1.66\%$ of CD14+/CD16+) and CD15+/CD16+ granulocytes ($7.95 \pm 6.46\%$) (Fig. 1h, i and j).

$\text{Angio}^{\text{PRP}}$ promotes angiogenesis and increases the wound healing of damaged organotypic human skin.

In view of the presence of CD146+/90+/31+ EPC in $\text{Angio}^{\text{PRP}}$, we evaluated the co-expression of CD34 and CD14 in EPC and non-EPC populations to better remark the presence of endothelial progenitor cells only in EPC (CD34+/14- $11.96 \pm 4.94\%$ for EPCs versus $0.23 \pm 0.29\%$ for non-EPCs; CD34+/14+ $13.85 \pm 7.46\%$ for EPCs versus $0.14 \pm 0.09\%$ for non-EPCs Fig. 1k). To assess angiogenic activities of $\text{Angio}^{\text{PRP}}$, EPC-CFA was used to monitor two different types of EPC-CFUs, pEPC-CFUs, and dEPC-CFUs which comprised small and large cells respectively. pEPCs derive from relatively immature, highly proliferative EPCs whereas dEPCs are relatively mature, differentiated, and able to promote EPC-mediated cell functions required for angiogenesis [39]. In addition, the expression of eNos and VE-Cadherin endothelial markers was higher in dEPCs compared to pEPCs ($85.82 \pm 2.08\%$ versus $64.62 \pm 3.49\%$ for eNOS and $85.82 \pm 1.23\%$ versus $70.06 \pm 2.4\%$ for VE-Cadherin, Fig. 1l). Colony-forming cells (CFCs) from 5×10^4 cells/dish of $\text{Angio}^{\text{PRP}}$ generated 2.9 ± 1.7 pEPC and 2.0 ± 1.2 dEPC colonies per dish, corresponding to 58.67% and 41.33% of the total number of colonies (Fig. 1m). To better evaluate the ability to undergo angiogenesis, we also performed an in vitro tube formation assay; HUVEC seeded on Matrigel with $\text{Angio}^{\text{PRP}}$ or PRP displayed capillary-like tubular structures after 24 hours (Fig. 1n). Quantitative analysis of capillary-like tubular structures showed significant increase of the total ramification length per field in $\text{Angio}^{\text{PRP}}$ ($33,780 \pm 3,530 \times 10^3 \mu\text{m}$) compared to PRP ($25,041 \pm 1,060 \times 10^3 \mu\text{m}$) (t-test * $p < 0.05$, Fig. 1o). All these data suggest a more efficient ability of $\text{Angio}^{\text{PRP}}$ to promote and participate to angiogenesis. Since

we found Tang subpopulation in Angio^{PRP} product, we evaluated whether Tang cells could have participated in EPC-CFA; the absence of a correlation between the number of EPC-CFUs observed and the percentage of Tang in individual samples confirmed that EPCs were the main cellular component involved in the angiogenesis process. (Spearman correlation, $r=-0,01408$, $p = 0,9504$, Fig. 1p). In order to validate the effects of Angio^{PRP} on skin lesions, we performed an in vitro evaluation on reconstructed human skin (EpiDerm FT). A 5 mm diameter circular lesion was performed on organotypic skin samples and different conditions were tested. Wound healing was monitored daily and measured as percentage of lesion area closed. Epithelial cells shouldering the wound migrate to reseal the injured tissue express cytokeratin-14 whereas fibroblasts from dermis express vimentin (Fig. 2a). The Angio^{PRP} showed a complete healing 6 days post injury (DPI), while the treatment with PRP took one more day to reach the same results (Fig. 2a). The Angio^{cells} and PBS could not succeed the complete healing in one week (Fig. 2b). The epidermal thickness was measured along the skin sections stained with hematoxylin and eosin: in Angio^{PRP} treated skin at 7 DPI it was significantly higher than in PRP (two-way ANOVA analysis of variance with Bonferroni correction; $p < 0.01$), Angio^{cells} (two-way ANOVA analysis of variance with Bonferroni correction; $p < 0.001$) and PBS (two-way ANOVA analysis of variance with Bonferroni correction; $p < 0.0001$) treated skin sections (Fig. 2c). Moreover, the Angio^{PRP} treatment induced the formation of differentiated epithelium as shown by the presence of both cornified (Involucrin) and spinous (Cytokeratins 14) layers, whereas Angio^{cells} and PBS-treated skin showed a thin and incomplete epidermal layer (Fig. 2c). The quantification of cytokeratin 14 immunofluorescence along the skin slices confirmed a completely reconstructed epithelium only in Angio^{PRP} treated samples (Fig. 2d).

Angio^{PRP} accelerates wound healing in mouse.

In order to evaluate whether Angio^{PRP} has beneficial effects on the healing of the skin wounds, two full-thickness excisional wounds were produced on the dorsal skin of NOD.Cg-Prkdc^{Scid}/J mice, an animal model that support the engraftment of human cells. All treatments were performed at day of wounding. Firstly, we characterized the Angio^{PRP} response in mice by hematoxylin and eosin and immunostaining for re-epithelialization markers loricrin and cytokeratin 10 in wounds at timepoints throughout the repair process ($n = 3$ for each timepoint) (Figure S1a). PBS was applied on the second wound on each mouse as control. In these experiments we found that Angio^{PRP} treatment induces the formation of granulation tissue and proliferation of the wound edge keratinocytes after 14 days and a complete closure after 21 days (Figure S1a) confirmed by the presence of E-cadherin positive adherent junction throughout the original lesion (Figure S1b). We next examined for the effects of Angio^{PRP} treatment ($n = 10$) compared to the gold clinical standard of wound treatment based on the use of a dermal matrix named Hyalomatrix ($n = 10$). The groups received PBS treatment, served as controls on the second wound. Hyalomatrix is comprised of a wound contact layer made of hyaluronic acid with an outer barrier layer comprised of a semipermeable silicone. The dermal matrix contact layer of Hyalomatrix is biodegradable and acts as a 3-dimensional scaffold for cellular invasion and capillary growth [56]. Skin wounds were monitored during the 21 days after treatments (Fig. 3a) and measurements of wound areas showed that both PBS

and Hyalomatrix treatments significantly delayed wound healing compared to Angio^{PRP} (Fig. 3b). In detail, Angio^{PRP} induced a complete closure of the lesion at 21 DPI whereas Hyalomatrix and PBS showed a wound closure of 75–80% and 90% at the same DPI ($p < 0,0001$, one-way ANOVA analysis of variance with Bonferroni correction) (Fig. 3b). Delayed wound healing of PBS and Hyalomatrix treatments was also confirmed by the quantification of time needed for the achievement of 60% of wound closure (mean of 21 and 15 DPI respectively for PBS and Hyalomatrix vs 6,5/7 DPI for Angio^{PRP}: $p < 0,0001$ one-way analysis of variance (ANOVA) with Bonferroni correction). We next examined samples for epidermal differentiation and we found that skin treated with Angio^{PRP} showed a complete wound healing induced by fibroblast and keratinocytes proliferation and migration to the wound site (Fig. 3c and d). Notably, at day 21 post-wounding, treatment with Angio^{PRP} resulted in a better and uniform distribution of cytokeratin 10 expression along the entire basal layer wounds compared to Hyalomatrix and PBS-injected wounds (Fig. 3e). Moreover, the expression of cytokeratin 5 in granular layer wounds was even more uniform in Angio^{PRP} than Hyalomatrix and PBS-injected wounds (Fig. 3f). Of note, we observed comparable cytokeratin 5 and 10 expression between intact dorsal NOD.Cg-Prkdc^{Scid}/J skin (WT skin) (Figure S2) and Angio^{PRP} wounds (Fig. 3c). Loricrin immunostaining of the stratum corneum at 21 DPI depicted a complete re-epithelization in Angio^{PRP} wounds but not in Hyalomatrix and PBS-injected wounds (Fig. 3c and d and Figure S2). Our next target was to verify the extracellular matrix remodeling and the physical properties of treated wounds. Histochemical staining with orcein demonstrated an elastin composition of Angio^{PRP} treated wounds more similar to healthy skin than Hyalomatrix (Fig. 4a, b and Figure S2). Moreover, Hyalomatrix and PBS treated skin samples showed the presence of a granulomatous buildup of cells filling the wound bed (Fig. 4b, c and Figure S2). Additionally, Masson's trichrome staining revealed biomaterial fibers entrapment inside the lesion area of Hyalomatrix treated wound. (Fig. 4b left low panel and Figure S3). As collagen and elastin control the elasticity of the connective [57] we examined the expression pattern of type VI collagen in WT, Angio^{PRP}, Hyalomatrix and PBS-injected wounds. The immunofluorescence staining revealed that type VI collagen was most present in Angio^{PRP} wounds and WT skin than Hyalomatrix and PBS-injected wounds (unpaired t-test, $p < 0,05$) (Fig. 4d and Figure S2). We next examined the mechanical properties of WT skin compared to the Angio^{PRP}, Hyalomatrix and PBS-injected wounds. During mechanical testing, resistance to tension by fibrils results in the linear region of the stress–strain curve, the modulus of which is often defined as modulus of elasticity. Angio^{PRP} wounds showed similar modulus as compared with WT skin ($3 \text{ MPa} \pm 0,7$ and $3,1 \pm 0,7$). In contrast, a lower modulus of elasticity was found in Hyalomatrix and PBS-injected wounds ($0,3 \text{ MPa} \pm 0,3$ and $1,8 \text{ MPa} \pm 0,70$, respectively) (Fig. 4e). These changes are consistent with our observation of the delayed matrix remodeling in Hyalomatrix and PBS-injected wounds. Among enzymes and cytokines that regulate ECM expression at the transcriptional and posttranscriptional level, the TGF β 1 figures as prominent regulator [58]. Western blot quantification showed decreased TGF β 1 expression 21 days after wounding in Angio^{PRP} wounds, in contrast to the increase seen in TGF β 1 levels in regenerating Hyalomatrix and PBS wounds (Fig. 6a). Another matrix modulator involved in remodeling and maintaining connective tissue homeostasis is the β -catenin [59]. Angio^{PRP} wounds and WT skin

exhibit decreased β -catenin whereas wounds of Hyalomatrix and PBS showed an increased expression of this mediator (Fig. 6a).

Angio^{PRP} reduced inflammation and promoted neoangiogenesis throughout the repair of skin mouse wounds.

To better characterize the wounds closure and re-epithelialization observed in Angio^{PRP}-treated wounds, we extended our observations to target the inflammation and angiogenesis in NOD.Cg-Prkdc^{Scid}/J mouse wounds 21 days after injury. The immunofluorescence staining of Angio^{PRP}-treated wounds for neutrophils with anti-Ly6G antibody revealed a significant decrease of these cells compared to the Hyalomatrix and PBS-treated wounds where we found exuberant accumulation of neutrophils (Fig. 5a). Consistently, we found increased number of CD206 + M2 macrophages in Hyalomatrix (one-way analysis of variance (ANOVA) with Bonferroni correction; $p < 0,01$) and partially in PBS-treated wounds (one-way analysis of variance (ANOVA) with Bonferroni correction; $p < 0,05$) (Fig. 5b and c). Since macrophages are required for wound vessel resolution, we characterized and quantified the number of CD31 positive capillaries and α -SMA positive vessel structures in treated wounds. Interestingly, Angio^{PRP} and WT skin displayed similar number of CD31 and α -SMA positive vessels (Fig. 5b, d and e) suggesting that blood vessels at Angio^{PRP} wounds moved back to uninjured WT skin levels. Otherwise, Hyalomatrix and PBS-treated wounds showed a reduced number of CD31 and α -SMA positive vessels compared to WT and Angio^{PRP} treated wounds, suggesting that Angio^{PRP} promotes angiogenesis in repairing skin tissues (one-way analysis of variance (ANOVA) with Bonferroni correction; $p < 0,01$ and $p < 0,05$ respectively) (Fig. 5b, d and e).

Molecular pathways involved in Angio^{PRP} wound healing.

We then determined the protein profile of Angio^{PRP}-treated wound by nLC-MS/MS analysis. To do this, we produced two full-thickness excisional wounds on the dorsal skin of NOD.Cg-Prkdc^{Scid}/J mice and each wound received the treatment or the PBS control. Wounds were divided in four groups (n = 10 each): Angio^{PRP} (group A), PBS-control of Angio^{PRP} (group C(A)), Hyalomatrix (group B) and PBS-control of Hyalomatrix (group C(B)). Dorsal WT skin from the same tested animal was analyzed as normal control profile (group D, n = 10). Total number of proteins identified was 1514, with a high technical and group reproducibility (Figure S4). Proteomic profiles of Hyalomatrix and PBS-control of Hyalomatrix wounds were markedly different compared to WT skin. Interestingly, Angio^{PRP} and PBS-control of Angio^{PRP} wounds showed similar cluster of principal components with higher correlations to WT skin (Fig. 6b). However, the differences in cluster pattern between PBS-control of Hyalomatrix and PBS-control of Angio^{PRP} wounds may suggest an unexpected systemic effect of Angio^{PRP} which may diffuse from the Angio^{PRP}-treated wound to the PBS-treated wound of the same animal. After Bonferroni correction, 179 proteins were differentially up- and down- regulated between Angio^{PRP} and Hyalomatrix-treated wounds (Fig. 7 and Figure S5). The Proteome recovery index (PRI) [53, 60] was then applied to identify the proteins involved in the wound recovery comparing all groups to the WT skin. Levels of 97 proteins were

recovered after Angio^{PRP} treatment (57 up-regulated and 40 down regulated), while only 23 were recovered after Hyalomatrix treatment (14 in common with Angio^{PRP} group) (Figures S6-9). Moreover, in Angio^{PRP}-treated wounds we identified 6 proteins that are recovered compared to the PBS-control of Hyalomatrix and 12 proteins down-regulated compared to the PBS-control of Angio^{PRP}. Clustering of normalized data confirmed that WT skin, Angio^{PRP} and PBS-control of Angio^{PRP} overlapped in the same macro group, distinct from the Hyalomatrix and PBS-control of Hyalomatrix that behave in a different cluster (Fig. 6b and c). We then evaluated the PPI metabolic functional modules identified using Cytoscape platform (Fig. 6d, Figures S6-9). Hyalomatrix and PBS-control of Hyalomatrix contained significantly up-regulated modules of serpins, proteins involved in defense response, cytoskeleton organization, complement and coagulation cascades, extracellular matrix (ECM) and ribosome (Figures S6-9). The group of WT skin, Angio^{PRP} and PBS-control of Angio^{PRP} included up-regulated keratins and proteins involved in lipid metabolism. Inside these networks depicting proteins up- or down-regulated, we identified a wound healing fingerprint of 17 Angio^{PRP}-related proteins that includes: caveolin-1 (CAV1), EGFR, fibronectin (FN1), decorin (DCN), plectin (PLEC), SERPINB2, prothrombin (F2), Heme Oxygenase 1 (HMOX1), Fibrinogen alpha-(FGA), beta- (FGB) and gamma- (FGG) chains, tenascin (TNC), plastin-2 (LCP1), alpha-tropomyosin (TPM1), cytokeratin-6A (KRT6A) and annexin A1 (ANXA1) (Fig. 6d and Figures S6-9). The expression of these wound healing proteins displays an opposite trend between Angio^{PRP} and PBS-treated wounds; DCN and TPM1 were up-regulated in Angio^{PRP}-treated wounds whereas FGA, FGB, FGG and F2 were up-regulated in PBS-treated wounds (Figures S6-9). Moreover, EGFR, FN1, TNC, ANXA1, FGG, FGA, FGB, F2, LCP1, KRT6A, TPM1 and HMOX1 were similar between WT skin and Angio^{PRP}-treated wounds. Of note, these proteins are differentially connected to the TGFβ1 and β-catenin-based signaling pathways that we found to be dominant in Hyalomatrix and PBS-treated wounds (Fig. 6a). Overall, these results indicate that Angio^{PRP} treatment modulates the CAV1 and EGFR/TGFβ/β-catenin pathways for a faster wound healing response.

Discussion

The physiological healing of wounds is governed by highly effective sequence of events that can be restricted by the extension of the affected area as well as by patient-related factors that include nutritional status, diabetes, pre-existing skin disease such psoriasis and genetic susceptibility [61, 62]. Different approaches are currently used, with a focus on the autologous products that offer a direct source of growth factors from patient's blood. Nowadays, the wound management is impacted by excessive costs and detrimental physical and psychological side effects for patients. Here, we developed a single-use, closed system that combines the cytokines and growth factors deriving from platelets, with a cell subpopulation characterized by angiogenic properties (Fig. 1). Therefore, our technology represents a low cost, accessible and clinically effective alternative to improve skin tissue regeneration.

We demonstrated that Angio^{PRP} provides positive regenerative outcomes with significantly accelerated wound healing. Herein, we demonstrated that Angio^{PRP}-induced metabolic signature is enriched in

proteins related to wound healing associated biological processes and, specifically, to signaling pathways driving extracellular matrix remodeling and TGF β 1/ β -catenin-based signaling pathways. Functionally, we reveal that Angio^{PRP} treatment promotes angiogenesis of HUVEC endothelial cells and activation of fibroblasts and keratinocytes, contributing to accelerate the wound healing of damaged organotypic human skin (Fig. 2). Moreover, the Angio^{PRP} rescued organotypic wounds area revealed the correct maturation of the spinous and cornified layers. In accordance with our findings, topical application of Angio^{PRP} in vivo showed beneficial effects. In fact, the results of in vivo study highlight the power of Angio^{PRP} treatment to enhance wound healing by promoting uniform regeneration of the basal and granular layers and vessel remodeling (Figs. 3, 5). Importantly, we coupled this effect with normalization of mechanical properties of rescued mouse wounds which is sustained by a correct arrangement of elastin and collagen fibers (Fig. 4). The network analysis-based protein–protein interactions of Angio^{PRP}-treated wounds showed up-regulation of decorin. Decorin and caveolin1 are inhibitors of the TGF- β 1 signaling pathway [63–65]. Moreover, caveolin1 negatively regulates β -catenin during wound healing [66]. Regardless, Angio^{PRP} wounds and WT skin exhibit similar decreased TGF β 1 and β -catenin levels (Fig. 6). In Angio^{PRP} network, we found another negative correlation between CAV1 and EGFR. EGFR itself is a central node in Angio^{PRP} network (Fig. 7) and it is known to have multiple roles in the regulation of healing processes [67]. Importantly, CAV1 is known to inhibit kinase activity of EGFR [68] and regulates degradation of RAC1 which is essential for EGFR-mediated fibroblast/keratinocytes migration.[69] Of note, caveolin regulates endothelial cells [70] and vessel remodeling upon mechanical stretch [27]. A link between CAV1 and fibronectin and fibrinogen in our protein–protein network points to their negative correlation. Indeed, CAV1 was recently shown to mediate fibronectin matrix assembly in fibroblasts [71] and fibrinogen is known to play a pivotal role in wound healing.[72] Upregulation of fibrinogen was shown to delay re-epithelialization and modulate angiogenesis [73]. However, modulation of fibrinogen/prothrombin pathway has been reported to induce changes in fibroblasts and keratinocytes proliferation in skin repair [74]. Consistent with delayed wound repair and enhanced fibroblast activity, we found in Hyalomatrix and PBS-control of Hyalomatrix wounds in vivo up regulation of fibrinogen, SERPINB2 and prothrombin proteins. Interestingly, TGF β 1 and β -catenin proteins are downregulated in both WT skin and Angio^{PRP}-treated wound (Fig. 6). Moreover, we coupled Angio^{PRP} effect with the acceleration of wound closure. Mechanistically, we reveal that recovered EGFR, FN1, TNC, ANXA1, FGG, FGA, FGB, F2, LCP1, KRT6A, TPM1 and HMOX1 proteins correspond to corrected wound closure, demonstrating their important role in the Angio^{PRP} molecular mechanism. Overall, these results have enabled us to provide a framework for how Angio^{PRP} supports wound healing, opening avenues for further clinical advances.

Conclusion

Over the past years, growth factors mediated by PRP and cell-based therapies were developed to improve wound healing. Unfortunately, clinical trials of single PRP or cell replacement treatments resulted in poor outcomes. Instead, a combined treatment composed of PRP and a pool of pro-angiogenic/keratogenic

cells may provide a more integrated method for a therapeutic approach to actively improve wound healing. The results of our study highlight the power of Angio^{PRP} treatment to enhance wound healing by promoting a cascade of events leading to the reduction of TGFβ1/β-catenin up-downstream signaling pathways. Taken together, we demonstrate that Angio^{PRP} retains a regenerative capacity by improving the wound repair and we provide insights into the Angio^{PRP} molecular mechanism opening new perspectives in the treatment of skin injuries.

Abbreviations

PRP Platelet-Rich Plasma

EGFR Epidermal Growth Factor Receptor

TGFβ Tissue Growth Factorβ

EPCs Endothelial Progenitor Cells

Tangs angiogenic T-cells

EPC-CFA Endothelial Progenitor Cell Colony-Forming Assay

SCF Stem Cell Factor

VEGF Vascular Endothelial Growth Factor

b-FGF basic Fibroblast Growth Factor

EGF Epidermal Growth Factor

IGF-1 Insulin Growth Factor 1

pEPC-CFUs primitive EPC Colony-Forming Units

dEPC-CFUs definitive EPC Colony-Forming Units

HUVECs Human Umbilical Vein Endothelial Cells

PBS Phosphate Buffered Saline

H&E Hematoxylin and Eosin

alpha SMA alpha Smooth Muscle Actin

TFA Trifluoroacetic Acid

FDR False Discovery Rates

PSM Peptide Spectrum Match

MAProMa Multidimensional Algorithm Protein Map

LDA Linear Discriminant Analysis

aSpC average Spectral Counts

DAve Differential Average

DCI Differential Confidence Index

PPI Protein-Protein Interaction

WBCs White Blood Cells

NKs Natural Killers

CFCs Colony-Forming Cells

DPI Days Post Injury

WT Wild Type

ECM Extracellular Matrix

One-way ANOVA one-way Analysis Of Variance

CAV1 Caveolin-1

FN1 Fibronectin

DCN Decorin

PLEC Plectin

SERPINB2 Serpin Family B Member 2

F2 Prothrombin

HMOX1 Heme Oxygenase 1

FGA Fibrinogen alpha

FGB Fibrinogen beta

FGG Fibrinogen gamma

TNC Tenascin

LCP1 Plastin-2

TPM1 alpha-Tropomyosin

KRT6A Cytokeratin-6A

ANXA1 Annexin A1

RAC1 Rac Family Small GTPase 1

Declarations

Ethics approval and consent to participate

The use of animals in this study was authorized by the National Ministry of Health (authorization number 51/2018-PR).

Peripheral blood was collected from healthy volunteers of the blood bank of Department of Transfusion Medicine and Haematology at Policlinico Hospital of Milan, after informed consent and according to the guidelines approved by the Ethics Committee on the Use of Human Subjects in Research of the Policlinico Hospital of Milan (Milan, Italy, Ethics Committee permission number 793/13)

Consent for publication

Not applicable

Availability of data and materials

The datasets during and/or analysed during the current study are available from the corresponding author on reasonable request.

Competing interests

S.E. and L.T. are employees of Novystem Spa and S.E. is an inventor on a related patent. M.B., M.M., D.D.S., A.D.P., R.J., E.F., L.P., E.T., G.R.M., P.M., Y.T. declare no competing interests.

Fundings

This research was funded by Novystem Spa, (Milan, Italy) and Italian Regenerative Medicine Infrastructure – IRMI of Ministero dell'Istruzione, dell'Università e della Ricerca (MIUR) D.D. prot. n. 257/Ric 30/05/2012. Funders of the study had no role in study design, data analysis, data interpretation, or writing of the report.

Author's Contributions

S.E., M.B. and L.T. conducted the experiments; S.E., M.B. and Y.T. designed the experiments; S.E., M.B., M.M. and Y.T analysed the results and wrote the article. L.P. and E.T performed cytometry experiments. D.D.S., A.D.P., E.F. and P.M. performed proteomic analysis. R.J. and G.R.M. contributed to animal model experiments.

Acknowledgements

Not applicable

References

1. Singer AJ, Clark RA. Cutaneous wound healing. *The New England journal of medicine*. 1999 Sep 2;341**10**:738-46. PubMed PMID: 10471461.
2. Sorg H, Tilkorn DJ, Hager S, Hauser J, Mirastschijski U. Skin Wound Healing: An Update on the Current Knowledge and Concepts. *Eur Surg Res*. 2017;58**1-2**:81-94. PubMed PMID: 27974711.
3. Jacinto A, Martinez-Arias A, Martin P. Mechanisms of epithelial fusion and repair. *Nat Cell Biol*. 2001 May;3**5**:E117-23. PubMed PMID: 11331897.
4. Eming SA, Krieg T, Davidson JM. Inflammation in wound repair: molecular and cellular mechanisms. *The Journal of investigative dermatology*. 2007 Mar;127**3**:514-25. PubMed PMID: 17299434.
5. Gurtner GC, Werner S, Barrandon Y, Longaker MT. Wound repair and regeneration. *Nature*. 2008 May 15;453**7193**:314-21. PubMed PMID: 18480812.
6. Kanji S, Das H. Advances of Stem Cell Therapeutics in Cutaneous Wound Healing and Regeneration. *Mediators Inflamm*. 2017;2017:5217967. PubMed PMID: 29213192. Pubmed Central PMCID: 5682068.
7. Richmond NA, Maderal AD, Vivas AC. Evidence-based management of common chronic lower extremity ulcers. *Dermatol Ther*. 2013 May-Jun;26**3**:187-96. PubMed PMID: 23742279.
8. Frykberg RG, Banks J. Challenges in the Treatment of Chronic Wounds. *Adv Wound Care (New Rochelle)*. 2015 Sep 1;4**9**:560-82. PubMed PMID: 26339534. Pubmed Central PMCID: 4528992.
9. Han G, Ceilley R. Chronic Wound Healing: A Review of Current Management and Treatments. *Advances in therapy*. 2017 Mar;34**3**:599-610. PubMed PMID: 28108895. Pubmed Central PMCID: 5350204.
10. Norman G, Westby MJ, Rithalia AD, Stubbs N, Soares MO, Dumville JC. Dressings and topical agents for treating venous leg ulcers. *The Cochrane database of systematic reviews*. 2018 Jun 15;6:CD012583. PubMed PMID: 29906322. Pubmed Central PMCID: 6513558.
11. Moues CM, Heule F, Hovius SE. A review of topical negative pressure therapy in wound healing: sufficient evidence? *Am J Surg*. 2011 Apr;201**4**:544-56. PubMed PMID: 21421104.
12. Gordon AJ, Alfonso AR, Nicholson J, Chiu ES. Evidence for Healing Diabetic Foot Ulcers With Biologic Skin Substitutes: A Systematic Review and Meta-Analysis. *Ann Plast Surg*. 2019 Oct;83**4S Suppl 1**:S31-S44. PubMed PMID: 31513064.

13. Kumar P. Classification of skin substitutes. *Burns*. 2008 Feb;341:148-9. PubMed PMID: 17869426.
14. Halim AS, Khoo TL, Mohd Yussof SJ. Biologic and synthetic skin substitutes: An overview. *Indian J Plast Surg*. 2010 Sep;43Suppl:S23-8. PubMed PMID: 21321652. Pubmed Central PMCID: 3038402.
15. Cervelli V, Bocchini I, Di Pasquali C, De Angelis B, Cervelli G, Curcio CB, et al. P.R.L. platelet rich lipotransfert: our experience and current state of art in the combined use of fat and PRP. *BioMed research international*. 2013;2013:434191. PubMed PMID: 24191244. Pubmed Central PMCID: 3804297.
16. Nicoli F, Balzani A, Lazzeri D, Gentile P, Chilgar RM, Di Pasquali C, et al. Severe hidradenitis suppurativa treatment using platelet-rich plasma gel and Hyalomatrix. *International wound journal*. 2015 Jun;123:338-43. PubMed PMID: 23834343.
17. Cervelli V, Lucarini L, Spallone D, Palla L, Colicchia GM, Gentile P, et al. Use of platelet-rich plasma and hyaluronic acid in the loss of substance with bone exposure. *Advances in skin & wound care*. 2011 Apr;244:176-81. PubMed PMID: 21422842.
18. Gentile P, Bottini DJ, Spallone D, Curcio BC, Cervelli V. Application of platelet-rich plasma in maxillofacial surgery: clinical evaluation. *The Journal of craniofacial surgery*. 2010 May;213:900-4. PubMed PMID: 20485077.
19. Gentile P, Calabrese C, De Angelis B, Dionisi L, Pizzicannella J, Kothari A, et al. Impact of the Different Preparation Methods to Obtain Autologous Non-Activated Platelet-Rich Plasma (A-PRP) and Activated Platelet-Rich Plasma (AA-PRP) in Plastic Surgery: Wound Healing and Hair Regrowth Evaluation. *International journal of molecular sciences*. 2020 Jan 9;212. PubMed PMID: 31936605. Pubmed Central PMCID: 7014364.
20. Gentile P, Garcovich S. Advances in Regenerative Stem Cell Therapy in Androgenic Alopecia and Hair Loss: Wnt pathway, Growth-Factor, and Mesenchymal Stem Cell Signaling Impact Analysis on Cell Growth and Hair Follicle Development. *Cells*. 2019 May 16;85. PubMed PMID: 31100937. Pubmed Central PMCID: 6562814.
21. Gentile P, Garcovich S. Systematic Review of Platelet-Rich Plasma Use in Androgenetic Alopecia Compared with Minoxidil((R)), Finasteride((R)), and Adult Stem Cell-Based Therapy. *International journal of molecular sciences*. 2020 Apr 13;218. PubMed PMID: 32295047. Pubmed Central PMCID: 7216252.
22. Gentile P, Scioli MG, Bielli A, De Angelis B, De Sio C, De Fazio D, et al. Platelet-Rich Plasma and Micrografts Enriched with Autologous Human Follicle Mesenchymal Stem Cells Improve Hair Regrowth in Androgenetic Alopecia. Biomolecular Pathway Analysis and Clinical Evaluation. *Biomedicines*. 2019 Apr 8;72. PubMed PMID: 30965624. Pubmed Central PMCID: 6631937.
23. Gentile P, Scioli MG, Bielli A, Orlandi A, Cervelli V. Concise Review: The Use of Adipose-Derived Stromal Vascular Fraction Cells and Platelet Rich Plasma in Regenerative Plastic Surgery. *Stem cells*. 2017 Jan;351:117-34. PubMed PMID: 27641055.
24. Scioli MG, Bielli A, Gentile P, Cervelli V, Orlandi A. Combined treatment with platelet-rich plasma and insulin favours chondrogenic and osteogenic differentiation of human adipose-derived stem cells in

- three-dimensional collagen scaffolds. *Journal of tissue engineering and regenerative medicine*. 2017 Aug;118:2398-410. PubMed PMID: 27074878.
25. De Angelis B, D'Autilio M, Orlandi F, Pepe G, Garcovich S, Scioli MG, et al. Wound Healing: In Vitro and In Vivo Evaluation of a Bio-Functionalized Scaffold Based on Hyaluronic Acid and Platelet-Rich Plasma in Chronic Ulcers. *Journal of clinical medicine*. 2019 Sep 18;89. PubMed PMID: 31540446. Pubmed Central PMCID: 6780765.
26. Beanes SR, Dang C, Soo C, Ting K. Skin repair and scar formation: the central role of TGF-beta. *Expert reviews in molecular medicine*. 2003 Mar 21;58:1-22. PubMed PMID: 14987411.
27. Peng Y, Huang S, Wu Y, Cheng B, Nie X, Liu H, et al. Platelet rich plasma clot releasate preconditioning induced PI3K/AKT/NFkappaB signaling enhances survival and regenerative function of rat bone marrow mesenchymal stem cells in hostile microenvironments. *Stem cells and development*. 2013 Dec 15;2224:3236-51. PubMed PMID: 23885779. Pubmed Central PMCID: 3868358.
28. Kaushik K, Das A. Endothelial progenitor cell therapy for chronic wound tissue regeneration. *Cytotherapy*. 2019 Nov;2111:1137-50. PubMed PMID: 31668487.
29. Menke NB, Ward KR, Witten TM, Bonchev DG, Diegelmann RF. Impaired wound healing. *Clinics in dermatology*. 2007 Jan-Feb;251:19-25. PubMed PMID: 17276197.
30. Suh W, Kim KL, Kim JM, Shin IS, Lee YS, Lee JY, et al. Transplantation of endothelial progenitor cells accelerates dermal wound healing with increased recruitment of monocytes/macrophages and neovascularization. *Stem cells*. 2005 Nov-Dec;2310:1571-8. PubMed PMID: 16081667.
31. Asahara T, Murohara T, Sullivan A, Silver M, van der Zee R, Li T, et al. Isolation of putative progenitor endothelial cells for angiogenesis. *Science*. 1997 Feb 14;2755302:964-7. PubMed PMID: 9020076.
32. Asahara T, Masuda H, Takahashi T, Kalka C, Pastore C, Silver M, et al. Bone marrow origin of endothelial progenitor cells responsible for postnatal vasculogenesis in physiological and pathological neovascularization. *Circulation research*. 1999 Aug 6;853:221-8. PubMed PMID: 10436164.
33. Rosenzweig A. Endothelial progenitor cells. *The New England journal of medicine*. 2003 Feb 13;3487:581-2. PubMed PMID: 12584365.
34. Hristov M, Weber C. Progenitor cell trafficking in the vascular wall. *Journal of thrombosis and haemostasis : JTH*. 2009 Jul;7 Suppl 1:31-4. PubMed PMID: 19630763.
35. Asahara T, Kawamoto A, Masuda H. Concise review: Circulating endothelial progenitor cells for vascular medicine. *Stem cells*. 2011 Nov;2911:1650-5. PubMed PMID: 21948649.
36. Manetti M, Pratesi S, Romano E, Bellando-Randone S, Rosa I, Guiducci S, et al. Angiogenic T cell expansion correlates with severity of peripheral vascular damage in systemic sclerosis. *PloS one*. 2017;128:e0183102. PubMed PMID: 28797111. Pubmed Central PMCID: 5552290.
37. Miao J, Qiu F, Li T, Zhao P, Zhang K, Lv M, et al. Circulating Angiogenic T Cells and Their Subpopulations in Patients with Systemic Lupus Erythematosus. *Mediators Inflamm*. 2016;2016:2842143. PubMed PMID: 27065298. Pubmed Central PMCID: 4811166.

38. Hur J, Yang HM, Yoon CH, Lee CS, Park KW, Kim JH, et al. Identification of a novel role of T cells in postnatal vasculogenesis: characterization of endothelial progenitor cell colonies. *Circulation*. 2007 Oct 9;116**15**:1671-82. PubMed PMID: 17909106.
39. Masuda H, Alev C, Akimaru H, Ito R, Shizuno T, Kobori M, et al. Methodological development of a clonogenic assay to determine endothelial progenitor cell potential. *Circulation research*. 2011 Jun 24;109**1**:20-37. PubMed PMID: 21566217.
40. Francescone RA, 3rd, Faibish M, Shao R. A Matrigel-based tube formation assay to assess the vasculogenic activity of tumor cells. *Journal of visualized experiments : JoVE*. 2011 Sep **755**. PubMed PMID: 21931289. Pubmed Central PMCID: 3230200.
41. Sebastiao MJ, Serra M, Pereira R, Palacios I, Gomes-Alves P, Alves PM. Human cardiac progenitor cell activation and regeneration mechanisms: exploring a novel myocardial ischemia/reperfusion in vitro model. *Stem cell research & therapy*. 2019 Mar 7;10**1**:77. PubMed PMID: 30845956. Pubmed Central PMCID: 6407246.
42. Black AT, Hayden PJ, Casillas RP, Heck DE, Gerecke DR, Sinko PJ, et al. Expression of proliferative and inflammatory markers in a full-thickness human skin equivalent following exposure to the model sulfur mustard vesicant, 2-chloroethyl ethyl sulfide. *Toxicology and applied pharmacology*. 2010 Dec 1;249**2**:178-87. PubMed PMID: 20840853. Pubmed Central PMCID: 2996832.
43. Belicchi M, Pisati F, Lopa R, Porretti L, Fortunato F, Sironi M, et al. Human skin-derived stem cells migrate throughout forebrain and differentiate into astrocytes after injection into adult mouse brain. *Journal of neuroscience research*. 2004 Aug 15;77**4**:475-86. PubMed PMID: 15264217.
44. Dunn L, Prosser HC, Tan JT, Vanags LZ, Ng MK, Bursill CA. Murine model of wound healing. *Journal of visualized experiments : JoVE*. 2013 May 28**75**:e50265. PubMed PMID: 23748713. Pubmed Central PMCID: 3724564.
45. Dias Gomes M, Letzian S, Saynisch M, Iden S. Polarity signaling ensures epidermal homeostasis by coupling cellular mechanics and genomic integrity. *Nature communications*. 2019 Jul 29;10**1**:3362. PubMed PMID: 31358743. Pubmed Central PMCID: 6662827.
46. Seifert AW, Kiama SG, Seifert MG, Goheen JR, Palmer TM, Maden M. Skin shedding and tissue regeneration in African spiny mice (*Acomys*). *Nature*. 2012 Sep 27;489**7417**:561-5. PubMed PMID: 23018966. Pubmed Central PMCID: 3480082.
47. Farini A, Gowran A, Bella P, Sitzia C, Scopece A, Castiglioni E, et al. Fibrosis Rescue Improves Cardiac Function in Dystrophin-Deficient Mice and Duchenne Patient-Specific Cardiomyocytes by Immunoproteasome Modulation. *The American journal of pathology*. 2019 Feb;189**2**:339-53. PubMed PMID: 30448404.
48. Nomura E, Katsuta K, Ueda T, Toriyama M, Mori T, Inagaki N. Acid-labile surfactant improves in-sodium dodecyl sulfate polyacrylamide gel protein digestion for matrix-assisted laser desorption/ionization mass spectrometric peptide mapping. *Journal of mass spectrometry : JMS*. 2004 Feb;39**2**:202-7. PubMed PMID: 14991690.

49. Sereni L, Castiello MC, Di Silvestre D, Della Valle P, Brombin C, Ferrua F, et al. Lentiviral gene therapy corrects platelet phenotype and function in patients with Wiskott-Aldrich syndrome. *The Journal of allergy and clinical immunology*. 2019 Sep;144**3**:825-38. PubMed PMID: 30926529. Pubmed Central PMCID: 6721834.
50. Kall L, Canterbury JD, Weston J, Noble WS, MacCoss MJ. Semi-supervised learning for peptide identification from shotgun proteomics datasets. *Nature methods*. 2007 Nov;4**11**:923-5. PubMed PMID: 17952086.
51. Mauri P, Deho G. A proteomic approach to the analysis of RNA degradosome composition in *Escherichia coli*. *Methods in enzymology*. 2008;447:99-117. PubMed PMID: 19161840.
52. Vigani G, Di Silvestre D, Agresta AM, Donnini S, Mauri P, Gehl C, et al. Molybdenum and iron mutually impact their homeostasis in cucumber (*Cucumis sativus*) plants. *The New phytologist*. 2017 Feb;213**3**:1222-41. PubMed PMID: 27735062.
53. Roffia V, De Palma A, Lonati C, Di Silvestre D, Rossi R, Mantero M, et al. Proteome Investigation of Rat Lungs subjected to Ex Vivo Perfusion (EVLP). *Molecules*. 2018 Nov 22;23**12**. PubMed PMID: 30467300. Pubmed Central PMCID: 6321151.
54. Bari E, Ferrarotti I, Di Silvestre D, Grisoli P, Barzon V, Balderacchi A, et al. Adipose Mesenchymal Extracellular Vesicles as Alpha-1-Antitrypsin Physiological Delivery Systems for Lung Regeneration. *Cells*. 2019 Aug 23;8**9**. PubMed PMID: 31450843. Pubmed Central PMCID: 6770759.
55. Maere S, Heymans K, Kuiper M. BiNGO: a Cytoscape plugin to assess overrepresentation of gene ontology categories in biological networks. *Bioinformatics*. 2005 Aug 15;21**16**:3448-9. PubMed PMID: 15972284.
56. Simman R, Mari W, Younes S, Wilson M. Use of Hyaluronic Acid-Based Biological Bilaminar Matrix in Wound Bed Preparation: A Case Series. *Eplasty*. 2018;18:e10. PubMed PMID: 29527248. Pubmed Central PMCID: 5828938.
57. Cavalcante FS, Ito S, Brewer K, Sakai H, Alencar AM, Almeida MP, et al. Mechanical interactions between collagen and proteoglycans: implications for the stability of lung tissue. *Journal of applied physiology*. 2005 Feb;98**2**:672-9. PubMed PMID: 15448123.
58. Kim LT, Yamada KM. The regulation of expression of integrin receptors. *Proceedings of the Society for Experimental Biology and Medicine Society for Experimental Biology and Medicine*. 1997 Feb;214**2**:123-31. PubMed PMID: 9034129.
59. Stojadinovic O, Brem H, Vouthounis C, Lee B, Fallon J, Stallcup M, et al. Molecular pathogenesis of chronic wounds: the role of beta-catenin and c-myc in the inhibition of epithelialization and wound healing. *The American journal of pathology*. 2005 Jul;167**1**:59-69. PubMed PMID: 15972952. Pubmed Central PMCID: 1603435.
60. Sereni L, Castiello MC, Marangoni F, Anselmo A, di Silvestre D, Motta S, et al. Autonomous role of Wiskott-Aldrich syndrome platelet deficiency in inducing autoimmunity and inflammation. *The Journal of allergy and clinical immunology*. 2018 Oct;142**4**:1272-84. PubMed PMID: 29421274. Pubmed Central PMCID: 6078823.

61. Anderson K, Hamm RL. Factors That Impair Wound Healing. *The journal of the American College of Clinical Wound Specialists*. 2012 Dec;**44**:84-91. PubMed PMID: 26199879. Pubmed Central PMCID: 4495737.
62. Eming SA, Martin P, Tomic-Canic M. Wound repair and regeneration: mechanisms, signaling, and translation. *Science translational medicine*. 2014 Dec 3;**6****265**:265sr6. PubMed PMID: 25473038. Pubmed Central PMCID: 4973620.
63. Iozzo RV, Sanderson RD. Proteoglycans in cancer biology, tumour microenvironment and angiogenesis. *Journal of cellular and molecular medicine*. 2011 May;**15**:1013-31. PubMed PMID: 21155971. Pubmed Central PMCID: 3633488.
64. Miyasato SK, Loeffler J, Shohet R, Zhang J, Lindsey M, Le Saux CJ. Caveolin-1 modulates TGF-beta1 signaling in cardiac remodeling. *Matrix biology : journal of the International Society for Matrix Biology*. 2011 Jun;**30****5-6**:318-29. PubMed PMID: 21641995. Pubmed Central PMCID: 4489541.
65. Tourkina E, Richard M, Gooz P, Bonner M, Pannu J, Harley R, et al. Antifibrotic properties of caveolin-1 scaffolding domain in vitro and in vivo. *American journal of physiology Lung cellular and molecular physiology*. 2008 May;**294****5**:L843-61. PubMed PMID: 18203815.
66. Egger AN, Rajabiestarabadi A, Williams NM, Resnik SR, Fox JD, Wong LL, et al. The importance of caveolins and caveolae to dermatology: Lessons from the caves and beyond. *Experimental dermatology*. 2020 Feb;**29****2**:136-48. PubMed PMID: 31845391. Pubmed Central PMCID: 7028117.
67. Repertinger SK, Campagnaro E, Fuhrman J, El-Abaseri T, Yuspa SH, Hansen LA. EGFR enhances early healing after cutaneous incisional wounding. *The Journal of investigative dermatology*. 2004 Nov;**123****5**:982-9. PubMed PMID: 15482488.
68. Mineo C, Gill GN, Anderson RG. Regulated migration of epidermal growth factor receptor from caveolae. *The Journal of biological chemistry*. 1999 Oct 22;**274****43**:30636-43. PubMed PMID: 10521449.
69. Nethe M, Anthony EC, Fernandez-Borja M, Dee R, Geerts D, Hensbergen PJ, et al. Focal-adhesion targeting links caveolin-1 to a Rac1-degradation pathway. *Journal of cell science*. 2010 Jun 1;**123****Pt 11**:1948-58. PubMed PMID: 20460433.
70. Gingras D, Gauthier F, Lamy S, Desrosiers RR, Beliveau R. Localization of RhoA GTPase to endothelial caveolae-enriched membrane domains. *Biochemical and biophysical research communications*. 1998 Jun 29;**247****3**:888-93. PubMed PMID: 9647788.
71. Monaghan-Benson E, Mastick CC, McKeown-Longo PJ. A dual role for caveolin-1 in the regulation of fibronectin matrix assembly by uPAR. *Journal of cell science*. 2008 Nov 15;**121****Pt 22**:3693-703. PubMed PMID: 18957516. Pubmed Central PMCID: 2586916.
72. Kubo M, Van de Water L, Plantefaber LC, Mosesson MW, Simon M, Tonnesen MG, et al. Fibrinogen and fibrin are anti-adhesive for keratinocytes: a mechanism for fibrin eschar slough during wound repair. *The Journal of investigative dermatology*. 2001 Dec;**117****6**:1369-81. PubMed PMID: 11886497.
73. Futagami A, Ishizaki M, Fukuda Y, Kawana S, Yamanaka N. Wound healing involves induction of cyclooxygenase-2 expression in rat skin. *Laboratory investigation; a journal of technical methods*

and pathology. 2002 Nov;8211:1503-13. PubMed PMID: 12429810.

74. Clark RA. Fibrin and wound healing. *Annals of the New York Academy of Sciences*. 2001;936:355-67. PubMed PMID: 11460492.

Figures

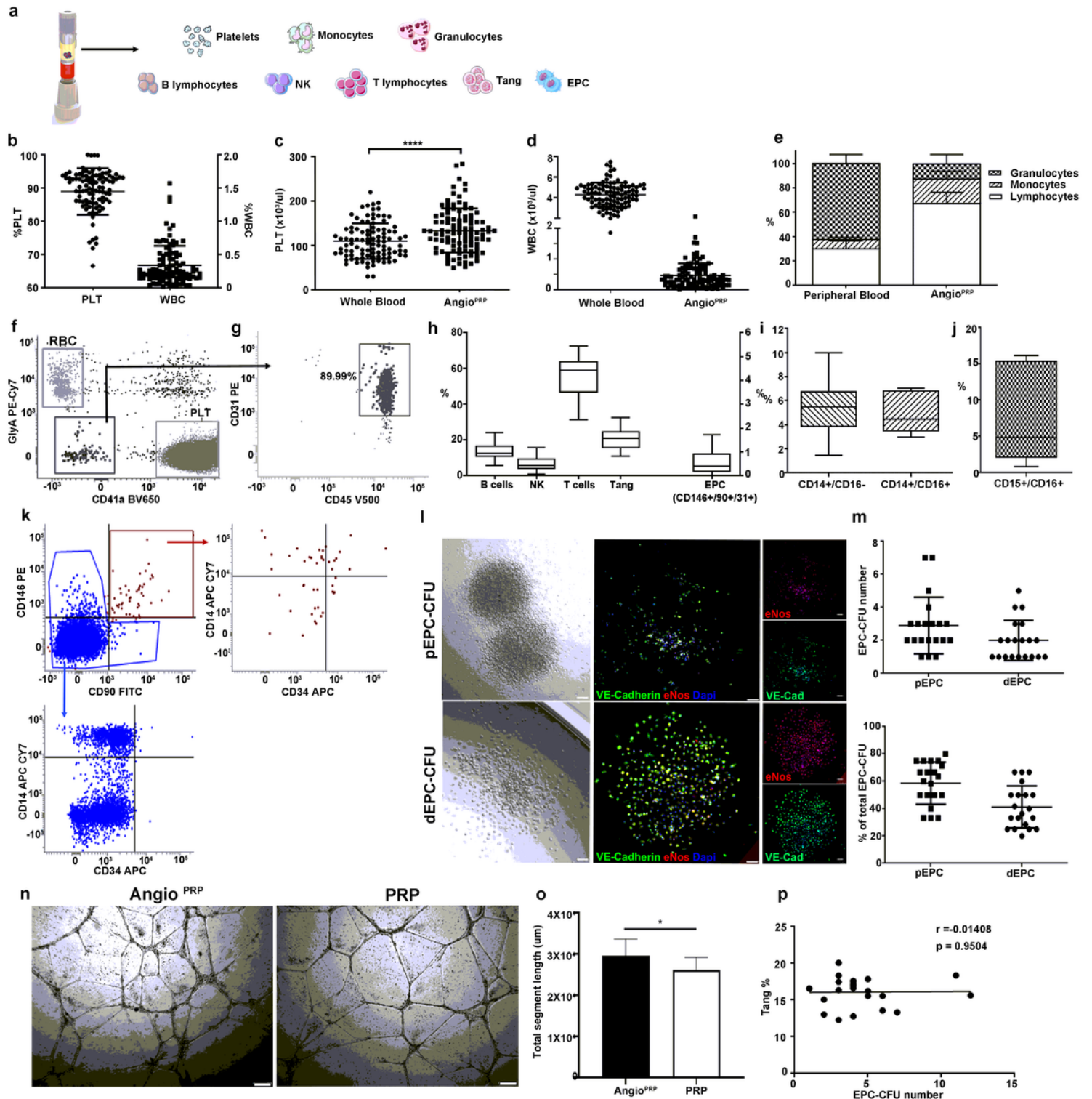


Figure 1

AngioPRP in vitro characterization, evaluation of in vitro cell vitality and angiogenic potential. (a) Schematic overview of the NovySep device and AngioPRP product. (b) Product composition, expressed as percentage of platelets and cells present in AngioPRP. Analysis of platelets enrichment (c) and WBC reduction (d) in AngioPRP, compared to original whole blood (unpaired t-test, $**p<0,01$). (e) Distribution of white blood cells (granulocytes, monocytes and lymphocytes percentages) in AngioPRP, compared to whole blood leukocyte formula. (f) Phenotypic characterization by flow cytometry of cellular component of AngioPRP. (g) Gated blood cells were characterized by CD31 and CD45 expression. (h) Flow cytometry quantification of B cells, NKs, T cells and Tang T cell sub-fraction (on left y-axis), and CD146+/90+/31+ EPC-like cells (on right y-axis) of AngioPRP. (i) Flow cytometry quantification of monocyte subpopulations of AngioPRP, expressed as CD14+/CD16+ and CD14+/CD16-. (j) Flow cytometry quantification of CD15+/CD16+ granulocyte subpopulation range present in AngioPRP. (k) Cytofluorimetric characterization of EPC and non-EPC fractions of AngioPRP. (l) Endothelial progenitor cell colony-forming assay (EPC-CFA) profile derived from AngioPRP; representative optical and immunofluorescence images of VE-cadherin (green) and eNOS (red) expression of small EPC colony forming unit (pEPC-CFUs) and large dEPC-CFUs in primary EPC-CFA at x10 magnification (scale bar = 250 μm). For fluorescence microscopy, nuclei were counterstained with DAPI and appeared in blue. (m) Quantification of pEPC and dEPC colonies obtained from AngioPRP expressed as number of colonies and percentages on total colonies. (n) Angiogenic assay performed in vitro on Matrigel: images of AngioPRP and PRP co-cultured with HUVEC cells after 24 hours (scale bar = 250 μm). (o) Quantification of total segment length of tubular structures evaluated by ImageJ and expressed as mean \pm SD (student t-test, $*p<0,05$). (p) Correlation by Spearman ranks test between number of EPC-CFUs and percentage of Tang subpopulation from individual donor samples.

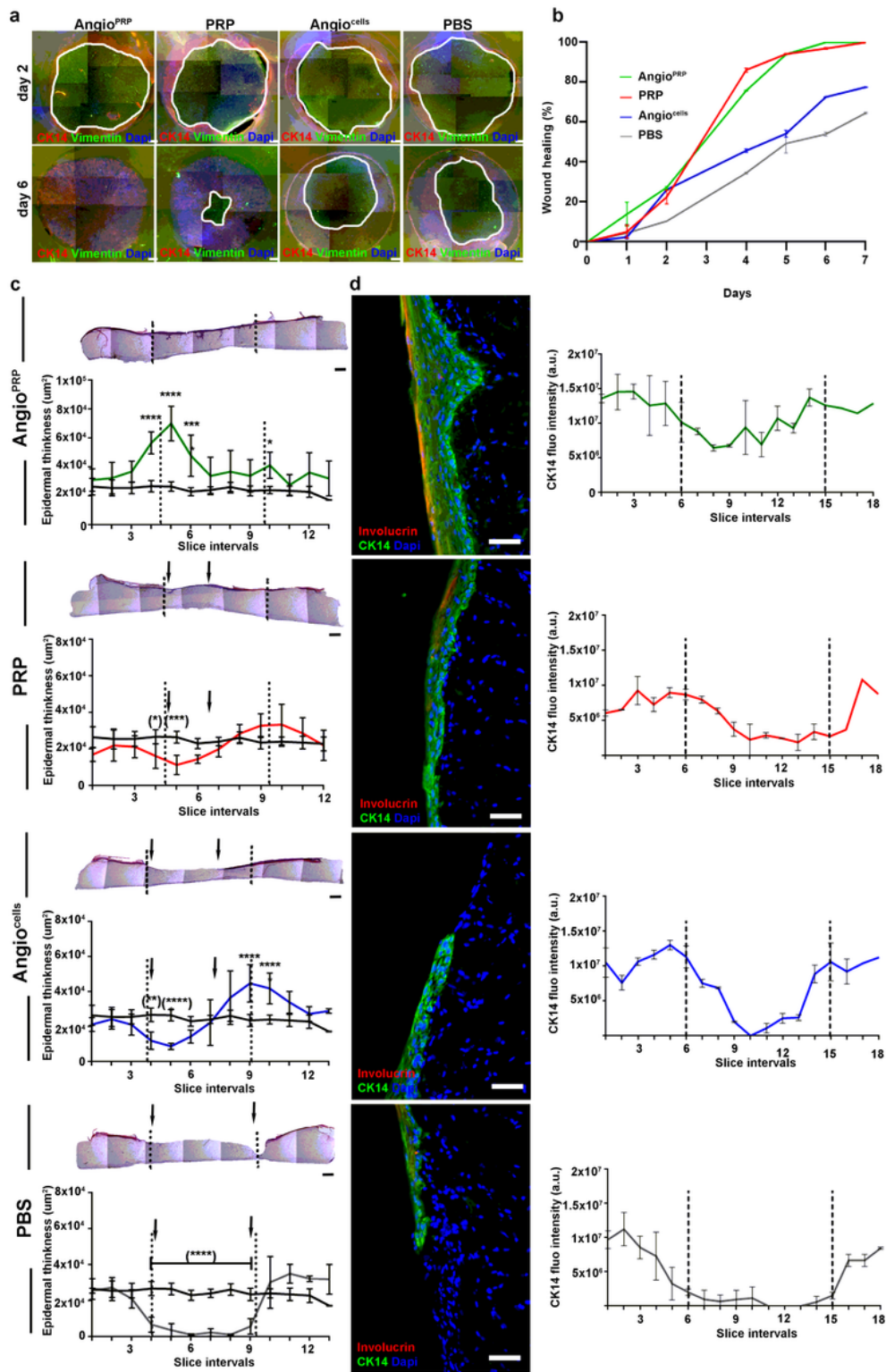


Figure 2

AngioPRP validation and epidermal differentiation on organotypic culture. (a) Representative immunofluorescence staining images showing restitution of organotypic 3D skin tissue after wounding with a biopsy punch (5 mm in diameter). Epithelial cells shouldering the wound migrate to reseal the injured tissue 2 and 6 days after treatment with AngioPRP, PRP, Angiocells and PBS (scale bar = 500 μ m). Migrating epithelial cells express cytokeratin-14 (red) and fibroblasts express vimentin (green); nuclei are

stained with DAPI (blue). (b) Quantification of wound healing trend as percentage of wound area closure. (c) Representative hematoxylin and eosin staining images of organotypic 3D skin section 7 days after treatment with AngioPRP PRP, Angiocells or PBS (scale bar = 500 μ m). Images were divided at 12 regular intervals (x-axis of relative graphics) representing the entire section and the epidermal thickness is quantified as area per interval. Epidermal thickness area quantification per interval of undamaged organotypic 3D skin is represented in black line as control. Dashed lines indicate the original wound boundary (5 mm-diameter excision); arrows show the lesion surface not yet re-epithelialized 7 days after wound. Data are presented as mean \pm SD. Two-way analysis of variance (ANOVA) with Bonferroni correction (*p<0,05, **p<0,01, ***p<0,001; ****p<0,0001) was performed comparing control (black line) to the AngioPRP (green line), PRP (red line), Angiocells (blue line) and PBS (grey line) epidermal thickness area. (d) Representative images of immunofluorescence staining for cytokeratin 14 (green) and involucrin (red) expression of organotypic 3D skin tissue section 7 days after AngioPRP, PRP, Angiocells or PBS treatments (scale bar = 75 μ m). Nuclei are stained with DAPI (blue). Cytokeratin 14 fluorescence intensity is measured for every single interval along the tissue slice and reported as consecutive points on x-axis (green line for AngioPRP, red line for PRP, blue line for Angiocells and grey line for PBS). Dashed lines represent the original wound boundary. Data are presented as mean \pm SD.

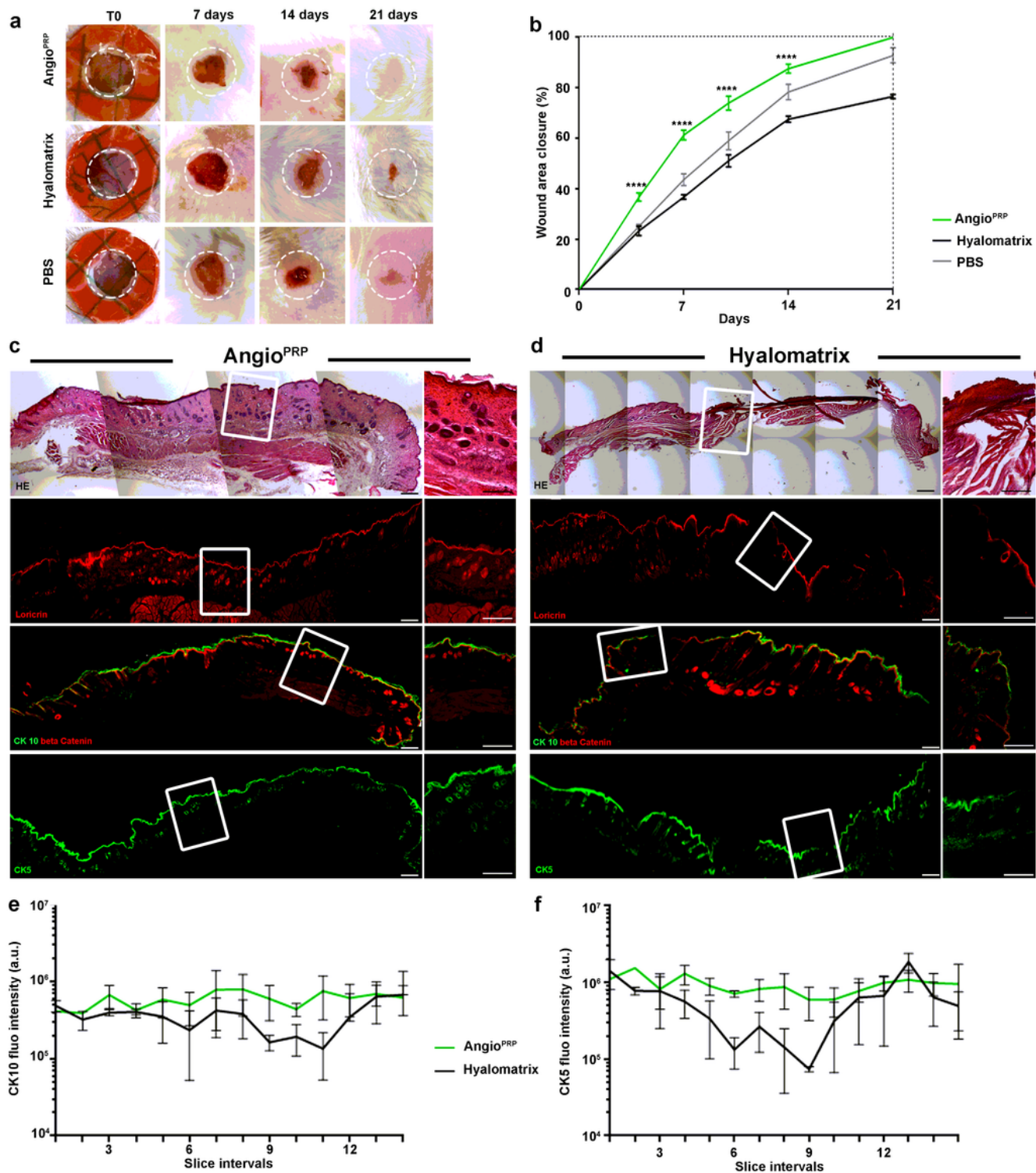


Figure 3

In vivo skin lesion closure and epidermal differentiation. (a) Representative images showing skin wound closure of the NOD.Cg-PrkdcScid/J at 0, 7, 14 and 21 days after wounding with a 5 mm biopsy punch (dashed white circle). (b) Wound closure rate is quantified as a ratio between the area measured and the area of the initial lesion at different timepoints (*** $p < 0.001$; **** $p < 0.0001$ one-way analysis of variance (ANOVA) Bonferroni correction). Hematoxylin and eosin histological reconstruction (scale bar = 500 μ m)

of skin section 21 days after AngioPRP (c) or Hyalomatrix (d) treatment (top panels, magnification scale bar = 200µm). Analysis of complete re-epithelization is performed by loricrin immunofluorescent staining (red, top immunofluorescence panels); cytokeratin 10 and β-catenin staining is performed to evaluate dermal-epidermal junction (central immunofluorescence panels) and cytokeratin 5 immunostaining for basal layer identification (lower immunofluorescence panels). Frame magnifications are reported in the enlarged images (scale bar = 200µm). Images were divided at 14-15 regular intervals (x-axis of relative graphics) representing the entire section and cytokeratin 10 (e) and cytokeratin 5 (f) fluorescence intensity quantification is represented for every single interval along the tissue slice and reported as consecutive points on x-axis (green line for AngioPRP, black line for Hyalomatrix). Data are presented as mean±SD.

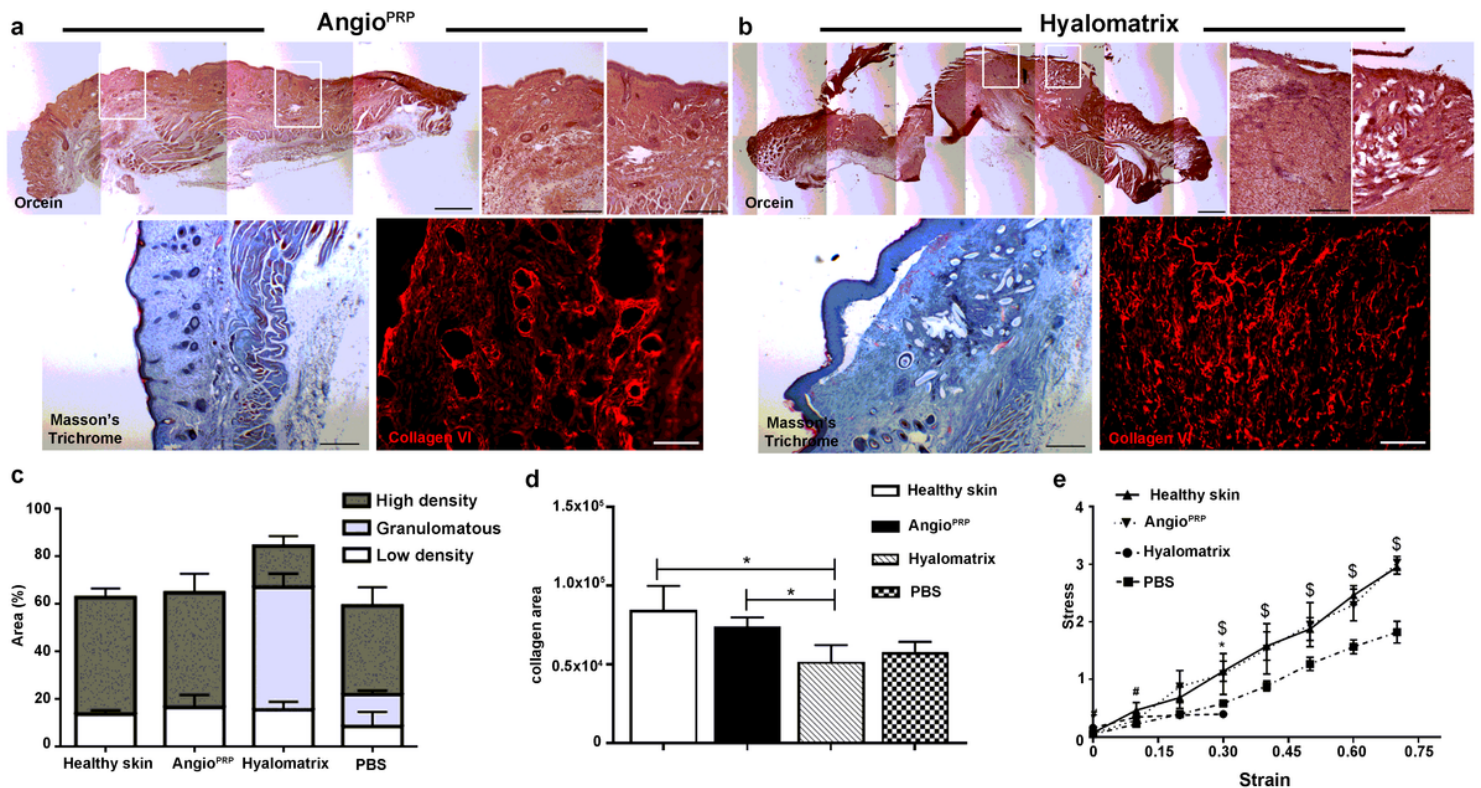


Figure 4

Skin elastic properties. Representative images of orcein histological staining of skin tissues of the NOD.Cg-PrkdcScid/J mice treated with AngioPRP (a) and Hyalomatrix (b) 21 days after wounding (scale bar = 500µm). Frame magnifications are shown in the enlarged images (top right panels of a and b, scale bar = 200µm); Masson's trichrome and collagen VI immunofluorescence stainings are shown in central panels of a and b (scale bar = 75µm). (c) Orcein staining quantification of high and low-density elastin and granulomatous area in skin tissues 21 day after treatment. Collagen VI area quantification is reported in d (unpaired t-test, *p<0,05). (e) Graphical representation of stress-strain curves obtained from dorsal skin analysis to determine mechanical properties of skin treated with AngioPRP and Hyalomatrix compared to PBS and healthy skin (unpaired t-test, *p<0,05).

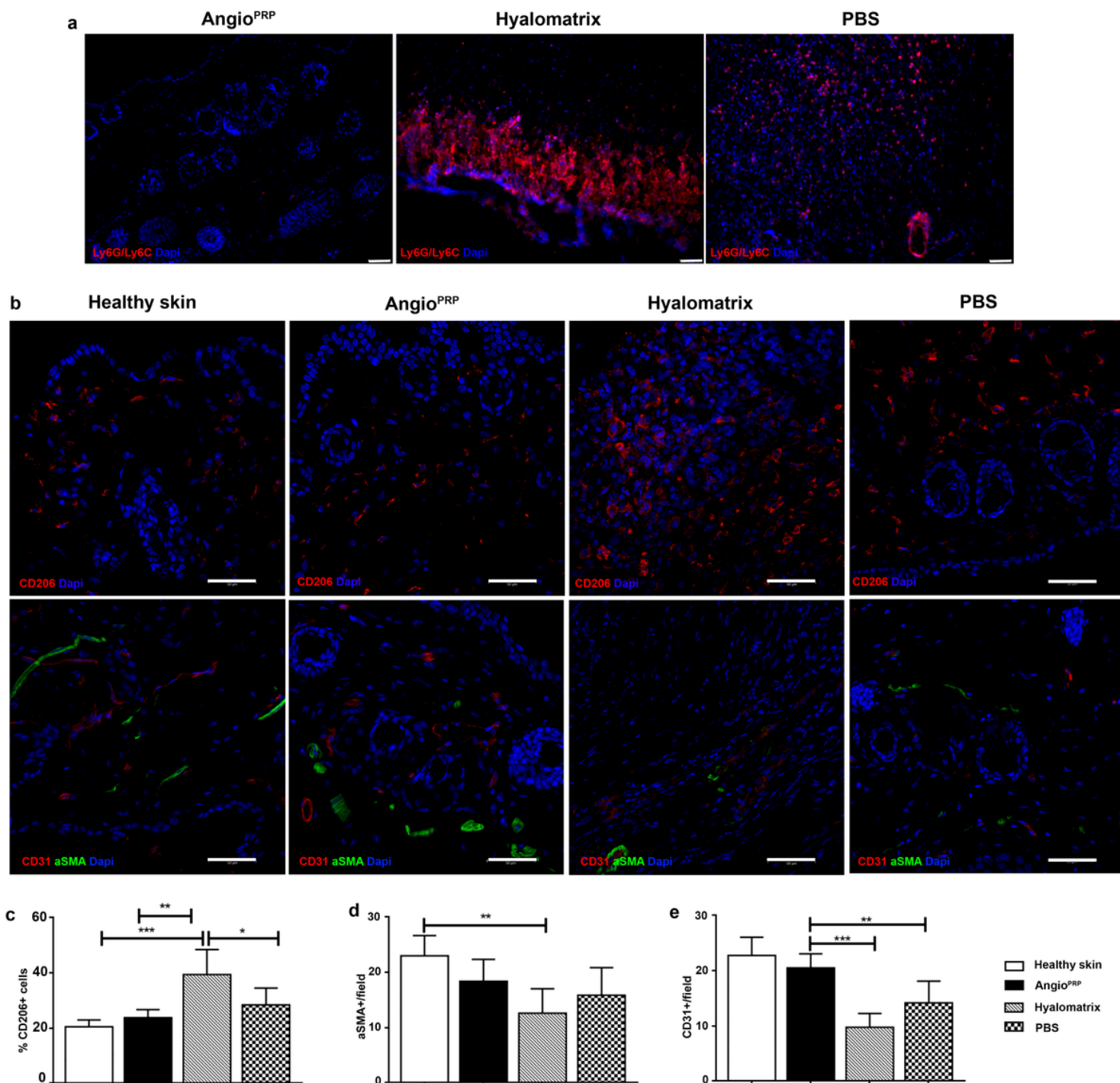


Figure 5

Inflammatory and vascularization processes. (a) Immunofluorescence staining of AngioPRP Hyalomatrix and PBS-treated wounds for neutrophils with anti-Ly6G antibody (scale bar = 50 μ m). (b) Immunofluorescence staining to detect inflammatory process of WT, AngioPRP, Hyalomatrix and PBS conditions 21 days after injury: M2 macrophages are identified by expression of CD206 antigen (scale bar = 75 μ m); angiogenic process is evaluated by CD31 (red) and α -SMA (green) immunofluorescence stainings (scale bar = 75 μ m). (c) Quantification of CD206 positive cells in healthy WT and AngioPRP, Hyalomatrix and PBS treated skin 21 days after injury, expressed as percentage (unpaired t-test, * $p < 0,05$

p<0,01; *p<0,001). Quantification of α -SMA (d) and CD31 (e) positive cells in healthy WT and AngioPRP, Hyalomatrix and PBS treated skin 21 days after injury, expressed as number counted in each field (unpaired t-test, **p<0,01; ***p<0,001).

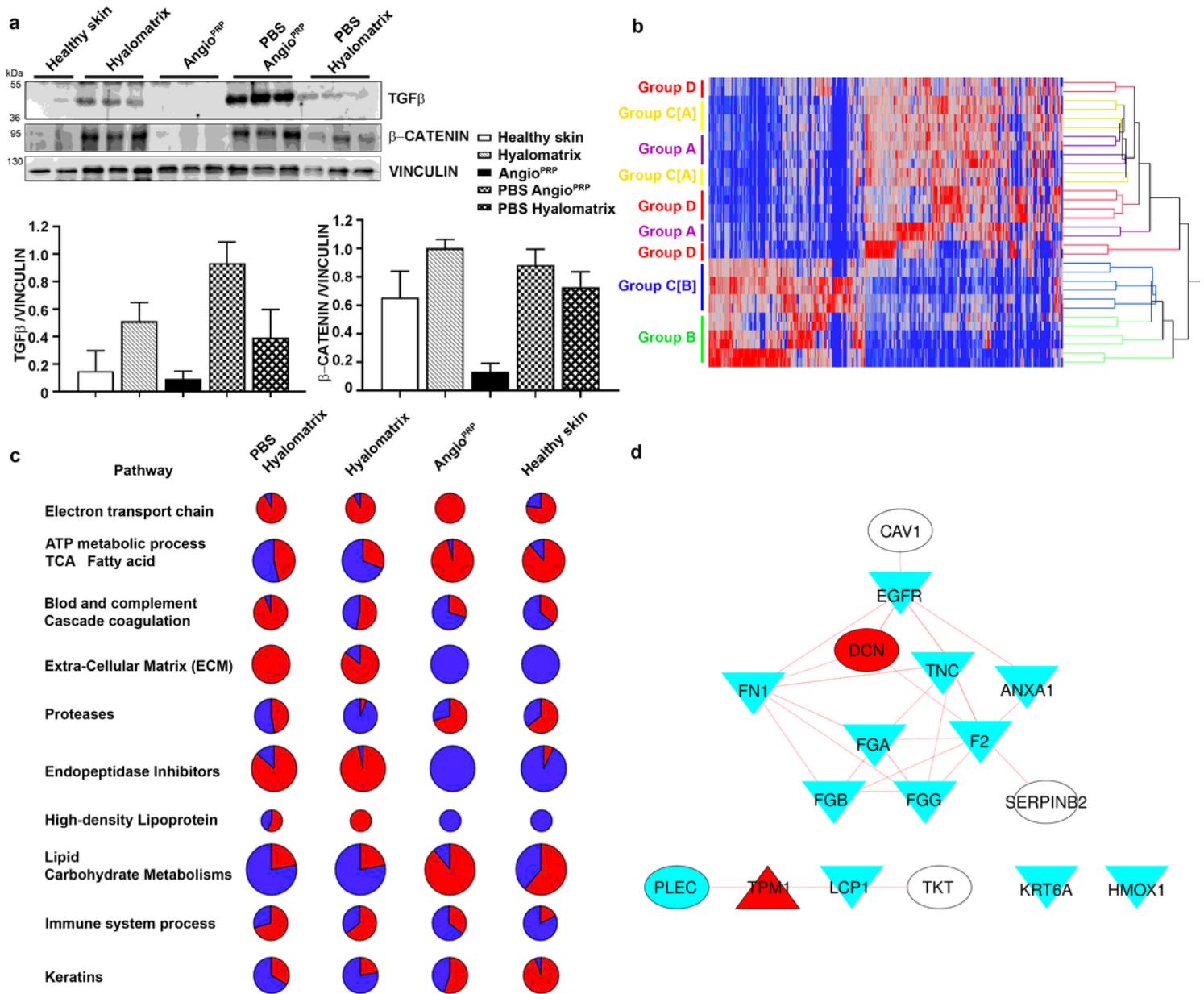


Figure 6

Molecular pathways involved in AngioPRP wound healing. (a) Western blot analysis of TGF β 1 and β -catenin in WT skin (Healthy), Hyalomatrix, AngioPRP, PBS-control of Hyalomatrix (PBS Hyalomatrix) and PBS-control of AngioPRP (PBS AngioPRP) wounds 21 days after injury. (b) Hierarchical clustering of proteins differentially expressed by comparing WT skin (D), Hyalomatrix (B), AngioPRP (A), PBS-control of Hyalomatrix (C(B)) and PBS-control of AngioPRP (C(A)) wounds 21 days after injury. Clustering was performed by computing the spectral count (SpC) value of proteins selected by linear discriminant analysis (LDA); Euclidean's distance metric and Ward's method were applied. The heatmap is related to the normalized aSpC (range 0–100) and indicates down-blue) and up-regulated (red) proteins,

Figure 7

Identification of protein networks of AngioPRP treated wound. Protein-protein interaction (PPI) network of proteins differentially expressed in AngioPRP condition 21 days after injury; PPIs retrieved by STRING Cytoscape's App, Score>0.15. E) Comparison of proteins involved in the wound healing pathways; color code corresponds to up- and down regulated proteins in disease, respectively; shape code correspond to recovering at WT level from PBS-control of Hyalomatrix due to AngioPRP treatment (down- and up arrows correspond to decreased and increased level, respectively).

Supplementary Files

This is a list of supplementary files associated with this preprint. Click to download.

- [FigureS1comp.tif](#)
- [FigureS2comp.tif](#)
- [FigureS3comp.tif](#)
- [FigureS4comp.tif](#)
- [FigureS5comp.tif](#)
- [FigureS6comp.tif](#)
- [FigureS7comp.tif](#)
- [FigureS8comp.tif](#)
- [FigureS9comp.tif](#)